HHS Public Access

Author manuscript

Nat Cell Biol. Author manuscript; available in PMC 2020 May 24.

Published in final edited form as:

Nat Cell Biol. 2019 June ; 21(6): 755–767. doi:10.1038/s41556-019-0329-y.

Non-canonical function of IRE1α determines mitochondria-associated endoplasmic reticulum composition to control calcium transfer and bioenergetics

Amado Carreras-Sureda[1,2,3], **Fabián Jaña**[2,4], **Hery Urra**[1,2,3], **Sylvere Durand**[5,6], **David E. Mortenson**[7], **Alfredo Sagredo**[1,2,3], **Galdo Bustos**[2,4,8], **Younis Hazari**[1,2,3], **Eva Ramos-Fernández**[9], **Maria L. Sassano**[10], **Philippe Pihán**[1,2,3], **Alexander R. van Vliet**[10], **Matías González-Quiroz**[1,2,3], **Angie K. Torres**[11], **Cheril Tapia-Rojas**[11], **Martijn Kerkhofs**[12], **Rubén Vicente**[13], **Randal J. Kaufman**[14], **Nibaldo C. Inestrosa**[9], **Christian Gonzalez-Billault**[2,15,16], **R. Luke Wiseman**[8], **Patrizia Agostinis**[10], **Geert Bultynck**[14], **Felipe A. Court**[2,8], **Guido Kroemer**[5,6,17,18,19], **J. César Cárdenas**[2,4,8,20], **Claudio Hetz**[1,2,3,15,21,*]

[1]Biomedical Neuroscience Institute, Faculty of Medicine, University of Chile, Santiago, Chile.

[2]FONDAP Geroscience Center for Brain Health and Metabolism, Santiago, Chile.

[3]Program of Cellular and Molecular Biology, Institute of Biomedical Sciences, University of Chile, Santiago, Chile.

[4]Anatomy and Developmental Biology Program, Institute of Biomedical Sciences, University of Chile, Santiago, Chile.

[5]Equipe Labellisée par la Ligue contre le cancer, Université Paris Descartes, Université Sorbonne Paris Cité, Université Paris Diderot, Sorbonne Université, INSERM U1138, Centre de Recherche des Cordeliers, Paris, France.

[6]Metabolomics and Cell Biology Platforms, Institut Gustave Roussy, Villejuif, France.

[7]Department of Molecular Medicine, The Scripps Research Institute, La Jolla, CA, USA.

[8]Center for Integrative Biology, Faculty of Sciences, Universidad Mayor, Santiago, Chile.

[9]Center for Aging and Regeneration, Department of Cell and Molecular Biology, Faculty of Biological Sciences, Pontifical Catholic University of Chile, Santiago, Chile.

[*]**Correspondence and requests for materials** should be addressed to C.H. chetz@hsph.harvard.edu.

Author contributions

C.H. and A.C.-S. designed the study. A.C.-S., F.J., H.U., S.D., D.E.M., A.S.-C., G.B., Y.H., E.R.-F., P.P., A.R.v.V., M.G.-Q., M.K., A.K.T., M.L.S., C.T.-R. and R.V. performed the experiments and analysed the data. A.C.-S., R.J.K., N.C.I., R.L.W., P.A., G.B., C.G.-B., F.A.C., G.K., J.C.C. and C.H., supervised the experiments and participated in their design. C.H. and A.C.-S. wrote the manuscript. All authors read and approved the final version of the manuscript.

Competing interests

The authors declare no competing interests.

Additional information

Supplementary information is available for this paper at https://doi.org/10.1038/s41556–019-0329-y.

Publisher's note: Springer Nature remains neutral with regard to jurisdictional claims in published maps and institutional affiliations.

Reprints and permissions information is available at www.nature.com/reprints.

online content

Any methods, additional references, Nature Research reporting summaries, source data, statements of code and data availability and associated accession codes are available at https://doi.org/10.1038/s41556–019-0329-y.

[10]Laboratory of Cell Death Research and Therapy, Department of Cellular and Molecular Medicine, VIB-KU Leuven Center for Cancer Biology, KU Leuven, Leuven, Belgium.

[11]Laboratory of Neurobiology of Aging, Centro de Biología Celular y Biomedicina, Facultad de Medicina y Ciencia, Universidad San Sebastián, Santiago, Chile.

[12]Laboratory of Molecular and Cellular Signaling, Department of Cellular and Molecular Medicine and Leuven Kanker Instituut, KU Leuven, Leuven, Belgium.

[13]Laboratory of Molecular Physiology, Department of Experimental and Health Sciences, Universitat Pompeu Fabra, Barcelona, Spain.

[14]Degenerative Diseases Program, Sanford Burnham Prebys Medical Discovery Institute, La Jolla, CA, USA.

[15]Buck Institute for Research on Aging, Novato, CA, USA.

[16]Department of Biology, Faculty of Sciences, University of Chile, Santiago, Chile.

[17]Pôle de Biologie, Hôpital Européen Georges Pompidou, AP-HP, Paris, France.

[18]Karolinska Institute, Department of Women's and Children's Health, Karolinska University Hospital, Stockholm, Sweden.

[19]Suzhou Institute for Systems Biology, Chinese Academy of Sciences, Suzhou, China.

[20]Department of Chemistry and Biochemistry, University of California, Santa Barbara, CA, USA.

[21]Department of Immunology and Infectious Diseases, Harvard School of Public Health, Boston, MA, USA.

Abstract

Mitochondria-associated membranes (MAMs) are central microdomains that fine-tune bioenergetics by the local transfer of calcium from the endoplasmic reticulum to the mitochondrial matrix. Here, we report an unexpected function of the endoplasmic reticulum stress transducer IRE1α as a structural determinant of MAMs that controls mitochondrial calcium uptake. IRE1α deficiency resulted in marked alterations in mitochondrial physiology and energy metabolism under resting conditions. IRE1α determined the distribution of inositol-1,4,5-trisphosphate receptors at MAMs by operating as a scaffold. Using mutagenesis analysis, we separated the housekeeping activity of IRE1α at MAMs from its canonical role in the unfolded protein response. These observations were validated in vivo in the liver of IRE1α conditional knockout mice, revealing broad implications for cellular metabolism. Our results support an alternative function of IRE1α in orchestrating the communication between the endoplasmic reticulum and mitochondria to sustain bioenergetics.

Cellular organelles are no longer conceived as unconnected structures with isolated functions, but as dynamic and integrated compartments. The best-characterized membrane contact sites bridge the endoplasmic reticulum (ER) and mitochondria[1]. The ER—the largest organelle in eukaryotic cells—controls protein folding, lipid synthesis and calcium storage. The folding capacity of the ER is constantly challenged by physiological demands and disease states. To sustain proteostasis, cells engage the unfolded protein response (UPR)[2], a

signalling pathway that enforces adaptive programs to adjust the secretory capacity, whereas uncompensated ER stress results in apoptosis[3]. Abnormal levels of ER stress are emerging as a driving factor for a wide variety of human diseases including diabetes, neurodegeneration and cancer[4].

The sites of physical communication between the ER and mitochondria are defined as mitochondria-associated membranes (MAMs), which form dynamic microdomains that are maintained by specialized tether and spacer proteins[5]. MAMs facilitate the transfer of calcium, phospholipids and metabolites between the two organelles[1]. The repertoire of signalling and metabolic proteins located at MAMs is determined by the local expression of chaperone proteins, such as the sigma-1 receptor (Sig-1R), among other components[6,7]. MAMs are central for the biogenesis of autophagosomes, as they determine the position of mitochondrial fission as well as influence the abundance and dynamics of organelles[8]. MAMs generate microdomains of localized calcium spikes released from the ER through inositol-1,4,5-trisphosphate ($InsP_3$) receptors ($InsP_3Rs$), thus stimulating calcium uptake by mitochondria[9]. Voltage-dependent anion channels (VDACs) are located at the outer mitochondrial membrane and mediate the internalization of calcium to reach a concentration that is suitable for transfer into the matrix[9,10]. Importantly, calcium uptake adjusts cellular metabolism as a cofactor of mitochondrial dehydrogenases during the production of NADH, and by increasing energy production through the activation of the tricarboxylic acid cycle (TCA)[10]. Conversely, abnormal fluctuations in mitochondrial calcium concentrations can trigger cell death[11].

The maintenance of stable contact sites between ER and mitochondria provides a platform for bidirectional crosstalk. Accumulating evidence suggests that disruption of MAMs perturbs ER physiology, leading to ER stress[12–15]. Interestingly, the UPR transducer PERK is enriched at MAMs[16] where it facilitates the tethering of the ER to mitochondria and sensitizes cells to apoptosis[16,17]. PERK signalling might also protect mitochondrial function under ER stress, possibly as an early adaptive mechanism[18]. IRE1α initiates the most conserved UPR signalling branch, controlling ER proteostasis and cell survival through distinct mechanisms[4]. IRE1α is a serine/threonine protein kinase and endoribonuclease that catalyses the unconventional processing of the mRNA that encodes X-Box binding protein-1 (XBP1), generating an active transcription factor termed XBP1s[19]. IRE1α also mediates the crosstalk with other alarm pathways by binding a series of adapter proteins[3]. A fraction of IRE1α is also located at MAMs, where stabilization by Sig-1R may enhance IRE1α signalling[20,21].

Here we investigated the contribution of IRE1α to the principal biological processes governed by the juxtaposition of ER and mitochondria. We identified a fundamental role for IRE1α in controlling the biology of MAMs, with broad implications for cellular metabolism. At the molecular level, the presence of IRE1α at MAMs determined the availability of $InsP_3R$, thus favouring calcium transfer to instigate mitochondrial respiration and ATP production. We provide mechanistic evidence that dissociates the canonical function of IRE1α as an UPR signal transducer from its structural role at MAMs as a scaffold. Together, our results indicate that IRE1α expression at MAMs adjusts cellular bioenergetics by fine-tuning the communication between the ER and mitochondria.

Results

Localization of IRE1α at MAMs and its impact on mitochondrial calcium transfer.

We performed density gradient centrifugations to collect cellular fractions enriched in mitochondria, ER and MAMs[22] to validate the presence of UPR signal transducers at MAMs. We confirmed an accumulation of IRE1α and PERK in MAM fractions from mouse embryonic fibroblasts (MEFs; Fig. 1a) and mouse livers (Fig. 1b).

To assess MAM function, we simultaneously monitored the release of ER calcium into the cytosol using Fura-2AM (Fura2) and mitochondrial calcium transfer using Rhodamine2N-AM (Rhod2) after the stimulation of cells with ATP to elicit $InsP_3$Rmediated responses. We used IRE1α knockout (KO) cells that were reconstituted with an haematoagglutinin (HA)-tagged form of IRE1α (IRE1α–HA), a strategy that fully restored UPR signalling[23] (Supplementary Fig. 1a). We also generated two sets of IRE1α null cells using CRISPR–Cas9 technology (Supplementary Fig. 1b,c). In all of these cellular systems, the ATP-dependent increase in cytosolic and mitochondrial calcium was reduced by ablating IRE1α expression (Fig. 1c–f, Supplementary Fig. 1d,e).

We then determined whether the alterations in calcium signalling observed in IRE1α-deficient cells were due to changes in the expression of calcium-handling proteins present in MAMs, including $InsP_3$R1, $InsP_3$R3, SERCA2b, MCU and VDAC1. We did not observe any significant changes in the basal expression of these proteins in IRE1α null cells (Fig. 1g, Supplementary Fig. 1f,g). Only a slight increase in MCU expression was detected in IRE1α CRISPR KO cells (Supplementary Fig. 1g). To increase $InsP_3$ inside the cell, we stimulated phospholipase C (PLC) using the chemical activator M3M3FBS[24], and observed decreased calcium release and mitochondrial uptake in IRE1α-deficient cells (Supplementary Fig. 1h,i). Similar results were obtained using a mitochondrial-targeted calcium indicator (CEPIA2mt[25]; Fig. 1h). Correlation analysis between ER calcium release and mitochondrial calcium uptake data suggested independent effects of IRE1α deficiency on both parameters (Fig. 1i, Supplementary Fig. 1j).

The alterations in ER calcium release caused by IRE1α deficiency can be explained by changes in the activity of $InsP_3$R and/ or altered steady-state luminal calcium content (which alters the calcium gradient)[26,27]. We investigated the effects of IRE1α expression on the activity of $InsP_3$R using a cell-free system. We stimulated permeabilized cells with $InsP_3$ after loading them with the calcium probe Mag-Fluo4. We observed a significant reduction in $InsP_3$Rmediated responses in IRE1α KO cells (Fig. 1j). We then performed measurements with radiolabelled calcium in permeabilized cells that were loaded with $^{45}Ca^{2+}$ to study different aspects of calcium homeostasis. Analysis of ER $^{45}Ca^{2+}$ loading indicated no significant differences between IRE1α null and IRE1α reconstituted cells (Supplementary Fig. 1k), suggesting unaltered steady-state luminal calcium levels. However, a slight enhancement in the kinetics of ER $^{45}Ca^{2+}$ loading (due to SERCA activity) was observed in IRE1αdeficient cells (Supplementary Fig. 1l), whereas passive leakage of calcium was unaltered (Supplementary Fig. 1m). Furthermore, cytosolic calcium levels were normal in IRE1α KO cells at resting conditions (Supplementary Fig. 1n). Taken together, these results uncovered a major role of IRE1α in the transfer of calcium into mitochondria.

IRE1α regulates mitochondrial bioenergetics and physiology.

As IRE1α influences mitochondrial calcium uptake, we assessed different parameters related to mitochondrial physiology and bioenergetics. Reduced mitochondrial membrane potential measured using tetramethylrhodamine methyl ester perchlorate (TMRM) was observed under normal cell culture conditions in IRE1α-deficient cells (Fig. 2a,b), correlating with a drop in ATP production (Fig. 2c,d, Supplementary Fig. 2a). To determine the site responsible for the failure in ATP synthesis, we used an ATP fluorescence resonance energy transfer (FRET)-based fusion protein that was tagged to the mitochondrial matrix or the cytosol[28]. A selective decrease in the mitochondrial pool of ATP was observed in IRE1α-deficient cells (Fig. 2e,f, Supplementary Fig. 2b).

We then monitored oxygen consumption using a Seahorse Analyzer. We observed a reduction in basal respiration, ATP coupling and maximal oxygen consumption rate in IRE1α-deficient cells (Fig. 2g,h). AMPK is a low-energy sensor that, once activated, phosphorylates several targets, which results in an increase in ATP generation and a reduction in ATP consumption[29]. Increased AMPK phosphorylation was observed in IRE1α-deficient cells under resting conditions (Fig. 2i, Supplementary Fig. 2c). Reduced calcium uptake into mitochondria is also associated with the activation of compensatory catabolic processes, such as autophagy, downstream of AMPK[30]. Targeting IRE1α expression increased basal LC3-II levels (Fig. 2j) and autophagic flux, which was measured by monitoring the distribution of LC3-II under nutrient starvation (Supplementary Fig. 2d). Consistent with this, inhibition of autophagy by blocking lysosomal function with chloroquine resulted in a further reduction in ATP levels in IRE1α-deficient cells (Supplementary Fig. 2e), indicating that these cells were suffering from metabolic stress.

ER–mitochondrial contact sites are known to determine the point of mitochondrial fission[31], and fused mitochondria are proposed to have a higher metabolic activity[32]. Transmission electron microscopy (TEM) indicated that IRE1α null cells contained smaller and more rounded mitochondria (Fig. 2k, Supplementary Fig. 2f). No changes in the content of ER was observed in the same experiments using two IRE1α null cell systems, whereas small alterations in ER complexity were detected in CRISPR KO cells (Supplementary Table 1). We complemented these experiments with live imaging of the ER marker KDEL–red fluorescent protein (RFP). This approach confirmed that the mean branch length of the ER was normal in IRE1α null cells, whereas the ER branch complexity (reflected by triple ER junctions) was slightly reduced (Supplementary Fig. 2g). Next, we assessed the shape of mitochondrial cristae using TEM because this morphological parameter correlates with mitochondrial respiration status[33]. We observed that IRE1α null cells exhibit an increased width of cristae (Supplementary Fig. 2h,i).

We then investigated the impact of IRE1α deficiency on MAM content. Increased colocalization between the ER marker ERp72 and the mitochondrial protein TOM20 was detected in IRE1α-deficient cells (Fig. 2l). We confirmed these observations using TEM by applying two strategies to quantify MAM morphometry (Fig. 2m, Supplementary Fig. 2j,k, Supplementary Table 2). These results suggest the presence of compensatory changes that balance the reduction in mitochondrial calcium uptake that is generated after the ablation of

IRE1α expression. Thus, IRE1α expression contributes to maintaining mitochondrial function in resting conditions.

IRE1α expression is required to increase metabolism in response to ER stress.

As IRE1α is a central component of the UPR, we investigated its contribution to metabolic control under ER stress. We confirmed the occurrence of a transient burst in ATP production during early responses to ER stress[34] (Supplementary Fig. 3a). However, this increase was almost absent in IRE1α-deficient cells (Supplementary Fig. 3a). Furthermore, ER stress stimulated an increase in the phosphorylation of AMPK over time (Supplementary Fig. 3b,c). By contrast, levels of phosphorylated AMPK (pAMPK) in IRE1α null cells were relatively high at basal ER stress levels and were insensitive to increases in ER stress (Supplementary Fig. 3b,c).

We then monitored whether the presence of IRE1α at MAMs was modulated by ER stress. Subcellular fractionation experiments did not indicate clear changes in the amount of IRE1α that was present at MAMs (Supplementary Fig. 3d). Quantitative colocalization of IRE1α–HA with either TOM20 or the MAM mask (corresponding to the overlap of ERp72 and TOM20) confirmed the presence of IRE1α at ER–mitochondria juxtapositions (Supplementary Fig. 3e). Treatment of cells with tunicamycin led to a slight enrichment of IRE1α at MAMs only after prolonged treatments (16 h; Supplementary Fig. 3e). These experiments suggest that the expression of IRE1α may also influence mitochondrial bioenergetics in the context of ER stress.

IRE1α controls the presence of $InsP_3R$ at MAMs.

We then studied the abundance of $InsP_3Rs$ in purified MAMs and observed a large reduction in IRE1α-deficient MEFs (Fig. 3a). Importantly, the total amount of $InsP_3Rs$ present in the input or the ER fraction remained unchanged when IRE1α expression was ablated (Fig. 1g, Supplementary Figs. 1f and 3f). We then evaluated the levels of $InsP_3Rs$ at ER–mitochondria juxtapositions using an in situ proximity ligation assay (PLA), a method that detects the presence of proteins within a range of 40 nm. Analysis of the proximity between VDAC1 and $InsP_3R1$ or $InsP_3R3$ indicated a strong reduction in PLA signals in IRE1α-deficient cells (Fig. 3b,c). Thus, our results suggest that IRE1α expression is necessary to locate $InsP_3Rs$ at MAMs.

Previous reports suggested that the distance between the ER and mitochondrial membrane is tightly controlled to allow the localization of $InsP_3R$ to MAMs[35], whereas greater distances impair calcium transfer into the mitochondrial matrix[36]. Analysis of the separation between the ER and the outer mitochondrial membrane using TEM revealed a narrower cleft in IRE1α-deficient cells (Fig. 3d,e). We validated these observations using a split green fluorescent proteinbased contact site sensor ($SPLICS_L$) that was designed to detect wide MAM contacts[37] (40–50 nm; Fig. 3f). We then expressed an artificial tether in IRE1α null cells to increase the separation between these organelles using a linker with nine tandem repeats (9xL), an approach that increased the cleft distance between the ER and the mitochondrial membrane (Fig. 3g, Supplementary Fig. 3g). However, this strategy did not recover the amount of $InsP_3R1$ at MAMs that was measured using PLA (Fig. 3h).

IRE1α physically interacts with $InsP_3R$ and controls mitochondrial calcium uptake independent of IRE1α enzymatic activity.

Next, we investigated whether the activities of IRE1α that are classically linked to the UPR are involved in the regulation of mitochondrial calcium uptake. We stably expressed different IRE1α mutants in IRE1α null cells including (1) an N-terminal deletion construct spanning the ER luminal domain (IRE1α-ΔN); (2) a C-terminal deletion mutant of the entire cytosolic region (IRE1α-ΔC); and (3) a non-dimerizing version (IRE1α-D123P) that is inactive and monomeric (Supplementary Fig. 4a). Functional evaluation of these mutants in calcium flux assays suggested that the C-terminal region of IRE1α enhances $InsP_3R$ activity, most probably through its monomeric inactive state (Supplementary Fig. 4b). We tested an additional mutation that affects the linker sequence (IRE1α-P830L), which lacks RNase and kinase functions[38] (Fig. 4a, Supplementary Fig. 4c). Notably, analysis of calcium transfer from the ER to the mitochondria indicated that the expression of IRE1α-P830L restored normal mitochondrial calcium uptake, similar to the wildtype construct (Fig. 4b) despite impaired XBP1 mRNA splicing (Fig. 4a). These results suggest that the function of IRE1α in mitochondrial calcium transfer can be separated from its canonical role as a UPR signal transducer.

To explore the possible function of IRE1α as a scaffold that may dock the $InsP_3R$ at MAMs, we tested the physical association between the two proteins. Immunoprecipitation experiments in HEK293T cells indicated a positive interaction between the proteins (Fig. 4c,d), which was fully ablated by deleting the cytosolic domain of IRE1α (Fig. 4e, Supplementary Fig. 4d). By contrast, the IRE1α-P830L and IRE1α-D123P mutants retained their ability to associate with $InsP_3R1$ (Supplementary Fig. 4e). The formation of a protein complex between IRE1α–HA and endogenous $InsP_3R1$ was also validated in MEFs (Fig. 4f). We also performed PLA experiments and confirmed the close proximity between IRE1α–HA and $InsP_3Rs$ in MEFs (Fig. 4g, Supplementary Fig. 4f).

We then purified recombinant fragments of the $InsP_3R1$ cytosolic domain as glutathione *S*-transferase (GST)-fusion proteins in bacteria to evaluate their binding to recombinant IRE1α-ΔN. Pulldown experiments revealed a tight association between IRE1α and domain 1 of $InsP_3R1$, as well as a weaker association with domain 3 (Fig. 4h). Domain 1 is important for $InsP_3R$ function, regulating its gating in response to $InsP_3$ (refs. [39,40]). Taken together, these experiments suggest that IRE1α controls mitochondrial calcium uptake independently of its enzymatic activities, and it is associated with the formation of a stable complex with $InsP_3Rs$ at basal levels.

Enforced expression of $InsP_3Rs$ rescues mitochondrial calcium uptake and ATP levels in IRE1α-deficient cells.

As the amount of $InsP_3Rs$ present in MAMs was reduced in IRE1α-deficient MEFs, we investigated whether the defects in mitochondrial function could be reverted by overexpressing $InsP_3Rs$. We stably transduced IRE1α KO cells with CRISPR activator (CRa) lentiviral particles to enhance the transcription of the endogenous $InsP_3R1$ gene (CRa-$InsP_3R1$; Fig. 5a,b). This approach augmented the presence of $InsP_3R1$ at MAMs in IRE1α null cells, as monitored using PLA (Fig. 5b), increasing mitochondrial calcium

uptake (Fig. 5c). Similar results were obtained when we evaluated ER–mitochondrial coupling by determining the correlation between cytosolic and mitochondrial calcium (Supplementary Fig. 5a). Consistent with these results, the mitochondrial membrane potential was increased in IRE1α deficient cells on CRa-InsP_3R1 expression (Fig. 5e), whereas AMPK phosphorylation was attenuated (Fig. 5f). Furthermore, CRaInsP_3R1 expression augmented steady-state ATP levels in IRE1α null cells (Fig. 5g). We complemented these experiments by generating CRa cells for InsP_3R3 (Fig. 5g) in which we observed improved levels of InsP_3R3 at MAMs (Supplementary Fig. 5b), increased ER–mitochondrial calcium transfer (Fig. 5h) and augmented basal ATP levels (Fig. 5i). Together, these results support a major role for the dysregulation of InsP_3R subtypes as a cause of mitochondrial physiology alterations generated by IRE1α deficiency.

IRE1α expression determines the presence of InsP_3R at MAMs in vivo.

To define the importance of IRE1α expression on MAM biology in vivo, we determined the consequences of genetically disrupting IRE1α in the mouse liver. We conditionally deleted *Ern1* (the gene that encodes IRE1α) using the Mx-Cre system, which is induced by an intraperitoneal injection of polyinosinic:polycytidylic acid (poly:IC) to ablate the target gene in the liver, and other tissues, of adult animals[41]. We used two independent floxed mouse strains that generate deletion mutants that flank the RNase domain (*Ern1*$^{\Delta R}$)[42] or the kinase domain (*Ern1*$^{\Delta K}$)[43] of IRE1α. A full impairment in the ability of IRE1α to induce XBP1 mRNA splicing was observed under experimental ER stress in both of these mouse models (Fig. 6a, Supplementary Fig. 6a). To evaluate the integrity of MAMs in *Ern1*$^{\Delta K}$ livers, we performed TEM studies to determine morphological parameters (Fig. 6b). An analysis of the content of MAMs and mitochondrial morphology indicated that mitochondria were smaller and showed a reduction in the distance between the ER and mitochondrial membrane (Fig. 6c,d). However, no differences in the length of MAMs or the circularity of mitochondria were observed (Fig. 6e,f).

Next, we determined the influence of IRE1α expression on the overall composition of MAMs by means of quantitative proteomics of purified subcellular fractions that we obtained from *Ern1* and *Ern1*$^{\Delta K}$ livers (Supplementary Fig. 6b). This unbiased approach identified the presence of 1,466 proteins in MAMs (Supplementary Table 3). This set of proteins greatly overlapped with a recent proteomic analysis of MAMs that were purified from mouse liver[44] and brain[45] (Supplementary Fig. 6b). We analysed the intersection between these three data sets (197 common proteins) with other hits obtained from the literature as canonical MAM proteins (19 proteins; Supplementary Table 4), resulting in a consensus of 216 MAMs proteins. A comparison of the MAM proteome between *Ern1*$^{\Delta K}$ and control livers indicated a significant reduction in the levels of InsP_3R1 in IRE1α mutant tissue, whereas InsP_3R3 was absent (Fig. 6g, Supplementary Table 3). Furthermore, we identified selective alterations in consensus MAM proteins, including changes in Tmed10, Aldh1l1, Apoc1 and Mccc2, whereas other canonical MAM markers such as calnexin, Sig-1R or VDAC1–3 remained unaltered (Fig. 6g,h; global data set and intersections in Supplementary Tables 3 and 4). Western blot analysis confirmed a robust reduction in the levels of InsP_3R1 in isolated MAM fractions (Fig. 6j), whereas InsP_3R1 expression in total liver extracts and ER fractions was comparable between both genotypes (Supplementary

Fig. 6c,d). Interestingly, an analysis of protein levels in the fractions suggested that *Ern1*$^{\Delta K}$ livers have a reduced quantity of MAM proteins but not mitochondrial proteins (Fig. 6k). Finally, an assessment of the possible interaction between IRE1α$^{\Delta K}$ and $InsP_3R1$ that used liver extracts revealed reduced coimmunoprecipitation (Fig. 6l). In contrast, analysis of liver samples from *Ern1*$^{\Delta R}$ mice showed no influence on the presence of $InsP_3R1$ in MAM-enriched fractions (Supplementary Fig. 6e). Taken together, these results suggest that IRE1α controls the composition of MAMs in vivo independently from its function as an ER stress transducer, because both KO models are deficient for UPR signalling but only IRE1α$^{\Delta K}$ affected $InsP_3R1$ distribution.

IRE1α deficiency alters mitochondrial metabolism in vivo.

To determine the consequences of IRE1α deficiency for global metabolism, we performed quantitative metabolomics of liver samples from both *Ern1*$^{\Delta K}$ and *Ern1*$^{\Delta R}$ mice. Among a total of 262 defined metabolites, our analysis retrieved 46 and 42 altered metabolites in *Ern1*$^{\Delta K}$ and *Ern1*$^{\Delta R}$ in mouse liver, respectively. We found only 15 metabolites that showed differences in both animal models (Supplementary Fig. 7a–c, Supplementary Table 5). A heat map and pathway analysis of the 31 metabolites that were specifically altered in *Ern1*$^{\Delta K}$ livers revealed clear perturbations to the TCA, glyoxylate and dicarboxylate metabolic pathways (Fig. 7a–c). An analysis of the TCA pathway in *Ern1*$^{\Delta K}$ livers indicated an accumulation of malate, fumarate, and citrate and isocitrate. Furthermore, we observed a reduction in the succinyl-CoA/succinate ratio (Fig. 7d), which might reflect a lower activity of isocitrate and α-ketoglutarate dehydrogenases, two enzymes that are regulated by calcium[46]. We also observed an increase in lactic acid in *Ern1*$^{\Delta K}$ livers, suggesting that a defect in the TCA cycle might be compensated by increasing glycolysis to maintain energetic homeostasis (Supplementary Fig. 7d). An analysis of ATP and reactive oxygen species (ROS; as a measure of electron chain transport activity) in liver homogenates and isolated mitochondria indicated comparable levels in *Ern1*$^{\Delta K}$ and littermate controls (Supplementary Fig. 7e,f), suggesting that the disruption of cellular organization was sufficient to ablate the effects of IRE1α expression on mitochondrial physiology.

Finally, due to the fact that the integrity of MAMs has been linked to the adjustment of glucose homeostasis, insulin signalling and obesity[47,48], we performed a glucose tolerance test in *Ern1*$^{\Delta K}$ mice. *Ern1*$^{\Delta K}$ animals presented reduced glucose clearance, suggesting deregulated energy control (Fig. 7f). Overall, our results indicate that IRE1α expression impacts global metabolism, an activity that can be dissociated from its canonical role as a UPR mediator.

Discussion

The control of cellular proteostasis and bioenergetics have historically been studied as separate processes. As many metabolic pathways are regulated at the ER, coordinated action with the mitochondria—the powerhouse of the cell—is tightly controlled to adjust energetic requirements according to need. Although the UPR has classically been linked to ER stress, increasing evidence suggests that the pathway has alternative functions in various cellular processes beyond secretory pathway surveillance[49]. The concept of the ‘UPRosome’ has

emerged[50], in which UPR signal transducers are viewed as platforms where distinct components assemble in a tissue-specific manner to integrate cellular physiology. This model prompted us to explore the importance of the abundance of IRE1α that is present at MAMs in calcium signalling and mitochondrial homeostasis.

Here we uncovered a contribution of IRE1α to the maintenance of MAM composition and function—the fine-tuning of mitochondrial respiration—at resting conditions. As a molecular intersection, IRE1α regulates the biology of $InsP_3Rs$ at different levels by influencing their localization at MAMs and their channel activity, which correlates with the formation of a protein complex between IRE1α and $InsP_3Rs$. Our genetic strategies unequivocally separated the effects that IRE1α exerts on ER–mitochondrial interactions from the known function of IRE1α in the UPR. We propose a model in which IRE1α operates as a scaffold that stabilizes $InsP_3Rs$ at MAMs (Fig. 7g). We speculate that the physical interaction of IRE1α with $InsP_3Rs$ may contribute to its docking at the MAM compartment and might allosterically modulate its activity, because domain 1 of the $InsP_3Rs$ is sensitive to $InsP_3$ and contains a calciumbinding site[40].

Calcium uptake into the mitochondrial matrix boosts oxidative phosphorylation as a cofactor of several metabolic enzymes of the TCA cycle[46]. The reduction in the rate of mitochondrial calcium uptake reported here in IRE1α KO MEFs might translate into a drop in ATP levels, engaging adaptive mechanisms to sustain cell survival, including the energy sensor AMPK, and the induction of catabolic processes such as autophagy. As IRE1α deficiency affected the expression of proteins related to phospholipid biosynthesis and metabolic enzymes at MAMs, the effects on energy metabolism and mitochondrial morphology described here cannot be exclusively limited to the consequences of IRE1α expression on the subcellular redistribution of $InsP_3R$. Overall, this study suggests that IRE1α has a housekeeping role in mediating ER-to-mitochondrion communication in the absence of ER stress.

The intersection of the UPR with inflammation, lipid metabolism, calcium homeostasis and energy control pathways is emerging as a major factor underlying metabolic diseases such as type 2 diabetes, insulin resistance and obesity[51]. Thus, components of the UPR machinery represent interesting targets to adjust energy metabolism and proteostasis control in a disease context. Interestingly, recent reports suggested that XBP1s regulates $InsP_3R$ expression[52], and also influences the influx of glutamine in T cells, having a negative effect on mitochondrial respiration[53], and suggesting that under ER stress multiple bioenergetics pathways could be fine-tuned downstream of IRE1α. Our results may have implications for metabolic syndromes and other pathological states that are linked to dysfunctional MAMs, including neurodegenerative diseases, immune disorders and cancer. It is conceivable that therapeutic interventions that target classical UPR signal transducers could affect cellular outputs well beyond proteostasis.

Methods

Cell culture, cell lines and DNA constructs.

All MEFs or HEK293 cells were maintained in DMEM medium that was supplemented with 5% fetal bovine serum (FBS) and non-essential amino acids, and grown at 37 °C with 5%

CO_2. IRE1α-deficient cells were described previously[54]. The production of amphotropic retroviruses using the HEK293 cell line was performed using standard methods[55]. IRE1α-deficient MEFs that were stably transduced with retroviral expression vectors for IRE1α–HA, IRE1α-D123P–HA, IRE1α-P830L–HA, IRE1α-ΔC– HA, IRE1α-ΔN–HA or an empty vector-expressing retrovirus were described previously[38,56]. In these constructs, IRE1α contains two tandem HA sequences at the C-terminal domain and a precision enzyme site before the HA tag. The control and 9xL linkers were provided by G. Hajnoczky. Alternatively, we generated CRISPR cells using a double nickase that was targeted to IRE1α or scrambled as a control (sc-429758-NIC and sc-437281; Santa Cruz). Two different sets of clones were prepared and a minimum of four clones (control and IRE1α, for each set) were screened for XBP1 mRNA splicing and the upregulation of BIP and CHOP (after experimental ER stress). CRISPR activation lentiviral particles that targeted $InsP_3R1$ and $InsP_3R3$ were generated in IRE1α KO cell lines following the manufacturer's instructions (sc-421192-LAC, sc-421194-LAC and sc-437282; Santa Cruz). All cell lines generated in this study, except for CRISPR KO cell lines, were pooled populations to avoid clonal effects.

Subcellular fractionation of MAMs and proteomic analysis.

Cellular or liver subcellular fractionation was performed by strictly following a previously reported protocol[22] with a variation consisting of the addition of an extra 15% Percoll gradient on top of the 30%. In brief, samples were washed and dounced in a stainless-steel Dura-Grind dounce tissue grinder (Wheaton). Cellular integrity was evaluated every five strokes after trypan blue staining. The homogenate was centrifuged two times at 640*g* to remove unbroken cells and nuclei. The supernatant was centrifuged twice at 9,000*g* to pellet liver crude mitochondria and twice at 7,000*g* and once at 10,000*g* for cells. The supernatant was centrifuged at 20,000*g* for 30 min, after which the obtained supernatant was further centrifuged at 100,000*g* to give a supernatant (cytosol) and a pellet (ER). Crude mitochondria were centrifuged 95,000*g* for 30 min on the top of a Percoll gradient (15–30%) to obtain MAMs (interphase) and the pure mitochondrial fraction (pellet). MAMs were pelleted after centrifugation at 100,000*g* for 1 h.

MAM lysates were washed by chloroform/methanol precipitation. Airdried pellets were resuspended in 1% RapiGest SF (Waters) and brought up in 100 mM HEPES (pH 8.0). Proteins were reduced using 5 mM Tris(2-carboxyethyl) phosphine hydrochloride (Thermo Fisher) for 30 min and alkylated with 10 mM iodoacetamide (Sigma-Aldrich) for 30 min at room temperature and protected from light. Proteins were digested for 18 h at 37 °C using 3 μg trypsin (Promega). After digestion, a 20 μg aliquot of peptides from each sample was reacted for 1 h with the appropriate TMT-NHS isobaric reagent (Thermo Fisher) in 40% (v/v) anhydrous acetonitrile and quenched with 0.4% NH_4HCO_3 for 1 h. Samples with different TMT labels were then pooled and acidified using 5% formic acid. Acetonitrile was evaporated on a SpeedVac and debris was removed by centrifugation for 30 min at 18,000*g*. Multi-Dimensional Protein Identification Technology (MuDPIT) microcolumns were prepared as described[57]. Liquid chromatography-mass spectrometry LC–MS analysis was performed using a Q Exactive mass spectrometer equipped with an EASY nLC 1000 (Thermo Fisher). MuDPIT experiments were performed by 5 min sequential injections of 0, 20, 50, 80 and 100% of buffer C (500 mM ammonium acetate in buffer A (95% water, 5%

acetonitrile, 0.1% formic acid)) and a final step of 90% buffer C and 10% buffer B (20% water, 80% acetonitrile, 0.1% formic acid, v/v/v) and each step was followed by a gradient from buffer A to buffer B. Electrospray was performed directly from the analytical column by applying a voltage of 2.5 kV with an inlet capillary temperature of 275 °C. Data-dependent acquisition of MS spectra was performed using the following settings: eluted peptides were scanned from 400 to 1,800 *m*/*z* with a resolution of 30,000 and the mass spectrometer was set in a data-dependent acquisition mode. The top ten peaks for each full scan were fragmented by higher energy collisional dissociation (HCD) using a normalized collision energy of 30%, a 100 ms activation time, a resolution of 7,500 and scanned from 100 to 1,800 *m*/*z*. Dynamic exclusion parameters were 1 repeat count, 30 ms repeat duration, 500 exclusion list size, 120 s exclusion duration, and exclusion width between 0.51 and 1.51. Peptide identification and protein quantification was performed using the Integrated Proteomics Pipeline Suite (IP2, Integrated Proteomics Applications Inc.) as previously described[57].

RNA isolation and PCR.

Semi-quantitative PCR primers for the *Xbp1* mRNA splicing were as follows: 5′-AAGAACACGCTTGGGAATGG-3′ and 5′-CTGCACCTGCTGCGGAC-3′. The full description of this assay was described previously[23].

Western blot analysis.

Cells were collected and homogenized in RIPA buffer (20 mM Tris pH 8.0, 150 mM NaCl, 0.1% sodium dodecyl sulphate (SDS), 0.5% Triton X-100) containing a protease inhibitor cocktail (Roche) in the presence of 50 mM NaF and 1 mM Na_3VO_4. Protein concentration was determined by micro-BCA assay (Pierce), and 50–100 μg of total protein was loaded onto SDS–polyacrylamide gel electrophoresis mini gels (Bio-Rad Laboratories) before transfer onto polyvinylidene difluoride (PVDF) membranes. Membranes were blocked using PBS, 0.02% Tween-20, 5% milk for 1 h at room temperature, then probed with primary antibodies. The following antibodies were used: anti-HSP90 (sc-13119, Santa-Cruz), anti-HA (715500, Invitrogen), anti-PERK (3192, CST), anti-VDAC1 (4866, CST), anti-$InsP_3R1$ (home-made antibody; Rbt03[58]); anti$InsP_3R3$ (610313, BD-Biosciences), anti-MCU (sc-246071, Santa-Cruz), antiSERCA2b (gift from P. Vangheluwe and F. Wuytack, K.U. Leuven)[59], anti-calnexin (SPA-860, Stressgene), anti-ECT complex (MS601/F1208, Mitosciences), anticytochrome *c* (ab110325, Abcam), anti-LC3B (2775S, CST), anti-actin (8691001, MP-Biomedicals), anti-pAMPK (2535, CST), anti-total AMPK (5832, CST), anti-γ-tubulin (sc-10732, Santa-Cruz), anti-GAPDH (sc-365062, Santa-Cruz) and anti-IRE1α (sc-20790, Santa-Cruz; and/or 3294, CST). Bound antibodies were detected using peroxidase-coupled secondary antibodies and the enhanced chemiluminescence (ECL) system.

Immunofluorescence, Duolink, SPLICS and TEM.

For immunofluorescence and Duolink experiments, cells were seeded on 12 mm cover slips. After the indicated transfections and treatments, cells were fixed for 20 min at room temperature using 4% paraformaldehyde and then permeabilized using 0.5% NP-40 in PBS containing 0.5% bovine serum albumin (BSA) for 10 min. After blocking for 1 h using 10%

FBS in PBS containing 0.5% BSA, cells were incubated with the indicated antibodies (also for PLA) anti-HA (901514, Biolegend or 9110, Abcam), anti-$InsP_3R1$ (ab5804, Abcam), anti-VDAC1 (ab14734, Abcam), anti-$InsP_3R3$ (610313, BD-Biosciences), anti-TOM20 (ab56783, Abcam), anti-ERp72 (SPS-720, Stressgene) or anti-LC3B (2775S, CST) overnight at 4 °C followed by either staining with Alexa-conjugated secondary antibodies (Molecular Probes) or following Duolink manufacturer's instructions as previously described (Duolink, Sigma-Aldrich)[23]. $SPLICS_L$ was transfected as previously described[37]. In brief, a 1:1 ratio for the OMM-GFP and ER-Long plasmid was used to visualize long MAM contacts (ranging from 40 to 50 nm). Images were acquired by confocal microscopy (Nikon C2 plus) using a ×60 oil objective lens. Images were stacked every 0.5 μm to cover all of the area of interest. Stacked images were deconvoluted using Huygens and ImageJ. Stacked deconvolved images were reduced to one dimension using the sumslices function (ImageJ). Colocalization was performed in thresholded images, and masked images were used to calculate Mander's/Pearson's index using ImageJ/NIS-elements. For $SPLICS_L$, convolved stacks were used to count objects from thresholded images in the three-dimensionally rendered image.

For TEM analysis, MEFs (control linker and 9xL were sorted for RFP) or liver samples (pre-perfused with PBS) were fixed 2 h using 2.5% glutaraldehyde, 0.01% picric acid and 0.1 M cacodylate buffer, pH 7.4. Samples were incubated in the same buffer with 1% OsO_4 for 1 h and then immersed in 2% uranyl acetate for 2 h, dehydrated in a gradient of ethanol and propylene oxide, and infiltrated in Epon (Ted Pella). Ultrathin sections were contrasted with 1% uranyl acetate and lead citrate. Grids were examined using a Philips Tecnai 12 electron microscope operated at 80 kV. TEM analysis was performed double blinded using ImageJ software. The analysis of MAM width was performed at a 40,000× amplification. MAMs with a maximal length (distance between membranes) of less than 30 nm were considered for study using TEM[36].

Calcium imaging, ER dynamics and mitochondrial membrane potential.

Cytosolic calcium signals were determined in MEFs loaded with 2.5 μM Fura2 (20 min at room temperature). Cytosolic [Ca^{2+}] increases are presented as the ratio of emitted fluorescence (510 nm) after excitation at 340 nm and 405 nm relative to the ratio measured before cell stimulation (Fura2 ratio 340/405). Simultaneous cytosolic and mitochondrial measurements were accomplished by loading cells with 1 μM Rhod2 for 30 min at 37 °C in 5% CO_2 before Fura2 incubation. Mitochondrial calcium increases are presented as the emitted fluorescence at 620 nm after stimulation with 560 nm, data were normalized to fluorescence levels before cell stimulation. Mitochondrial calcium entry was measured by transiently transfecting the CEPIA2mt calcium probe[25] and by exciting cells at 480 nm and recording emission at 525 nm. Mitochondrial membrane potential was measured by loading cells with 10 nM TMRM for 30 min at 37 °C 5% CO_2. Excitation at 525 nm and emission at 630 nm retrieved fluorescence intensity, indicative of mitochondrial voltage. ER dynamics were studied by transiently expressing KDEL– RFP in CRIPSR IRE1α-deficient cells. ER junctions and branching were evaluated as previously described[60].

Live imaging was carried out at room temperature using an Olympus IX81 inverted spinning microscope. Cells were incubated/bathed in a solution containing 140 mM NaCl, 5 mM KCl, 1.2 mM $CaCl_2$, 0.5 mM $MgCl_2$, 5 mM glucose, 10 mM HEPES (300 mosmol l^{-1}, pH 7.4 with Tris). Ca^{2+}-free solutions were obtained by replacing $CaCl_2$ with an equal amount of $MgCl_2$ plus 0.5 mM EGTA.

$InsP_3R$ activity was studied as previously described[61]. Cells were loaded with 20 μM Mag-Fluo4-AM in HEPES-buffered saline (135 mM NaCl, 5.9 mM KCl, 11.6 mM HEPES, 1.5 mM $CaCl_2$, 11.5 mM glucose, 1.2 mM $MgCl_2$, pH 7.4) with 1 mg ml^{-1} of BSA and 0.2 mg ml^{-1} of Pluronic F127 (Invitrogen). After 60 min, cells were permeabilized for 15 min in calcium-free cytosol-like medium (140 mM KCl, 20 mM NaCl, 1 mM EGTA, 2 mM $MgCl_2$, 20 mM Pipes, pH 7.0) containing 10 μg ml^{-1} of saponin. Subsequently, cells were resuspended in a cytosol-like medium without Mg^{+2}, supplemented with 10 μM FCCP and 220 nM free calcium. ER calcium loading was accomplished by adding 1.5 mM Mg-ATP. On maximal loading, 3 μM $InsP_3$ or 1 μM ionomycin (to induce the maximal response) were added to the cells. Results were calculated as $F_x - F_{200}$ of fluorescence emission at 525 nm after excitation at 490 nm. Percentage of response was calculated for every experiment compared to its ionomycin induced maximal release. Fluorescence was measured using a 96-well microplate reader with automated fluid additions at 37 °C (FlexStation 3, Molecular Devices).

Unidirectional $^{45}Ca^{2+}$ fluxes were performed in 12-well clusters on confluent monolayers of MEFs 5 d after plating the cells at 10,000–15,000 cells per well. The chemical composition of the permeabilization, loading and efflux media were described previously[62]. Cells were permealized using 20 μg ml^{-1} saponin for 10 min. Non-mitochondrial Ca^{2+} stores were loaded with 150 nM free Ca^{2+}, a mixture of $^{40}Ca^{2+}$ and $^{45}Ca^{2+}$ (final specific activity of 0.3 MBq ml^{-1}). To determine ER $^{45}Ca^{2+}$ uptake, loading was carried out at 30 °C for 5–10 min and for 45 min (to obtain steady-state levels) in the presence of 10 mM NaN_3 with or without 500 nM thapsigargin. Afterwards, cells were washed twice with efflux medium supplemented with thapsigargin. The $^{45}Ca^{2+}$ amount in the stores was released by adding 2% SDS for 30 min. This amount of $^{45}Ca^{2+}$, expressed in counters per minute A (CPMA), was then divided by the number of cells per well, as counted by the Invitrogen Countess II FL Automated Cell Counter. To assess the passive $^{45}Ca^{2+}$ leak from the ER, $^{45}Ca^{2+}$ loading was carried out for 45 min, then halted by two washes with efflux medium supplemented with thapsigargin. Next, efflux medium was provided and collected every 2 min (up to 18 min after initial collection) from each well. At the end of the experiment, 2% SDS was used to determine the remnant $^{45}Ca^{2+}$. This value was used to calculate the ER $^{45}Ca^{2+}$ content over time by adding it in retrograde order to the radioactivity collected during the successive time intervals.

Immunoprecipitation and pull-down assays.

Liver homogenates, transiently transfected HEK293 cells or indicated MEFs stably were prepared in lysis buffer (0.5% NP-40, 250 mM NaCl, 30 mM Tris, 0.5% glycerol, pH 7.4, 50 mM NaF, 1 mM Na_3VO_4, 250 mM phenylmethylsulfonyl fluoride (PMSF) and protease inhibitors). To immunoprecipitate HA-tagged IRE1α or endogenous IRE1α protein, extracts

were incubated with rat anti-HA (Roche) or anti-IRE1α (sc-20790, Santa Cruz) antibodies overnight at 4 °C under rotation, and then 30 μl of prewashed magnetic beads (1614013, Biorad) was added for 3 h at 4 °C. Beads were subsequently washed twice for 5 min with 1 ml of lysis buffer at 4 °C and then once in lysis buffer with 500 mM NaCl. Protein complexes were eluted by heating at 95 °C for 5 min in loading buffer with 100 mM dithiothreitol (DTT).

For GST pull-down experiments, GST-fusion constructs of different domains of $InsP_3R1$ were transformed into *Escherichia coli* BL21 (DE3) and induced with 0.1–1 mM isopropyl-β-d-thigalactopyranoside for 3–6 h and subsequently purified using glutathione sepharose beads (Thermo Scientific). For binding assays, 4 μg of different GST-tagged $InsP_3R1$ domains was incubated with approximately 4 μg of cytoplasmic domain of GST-tagged IRE1α for 6 h at 4 °C on an end-to-end rotor in binding buffer containing 0.2% Triton X-100, 50 mM Tris-Cl (pH 7.5), 100 mM NaCl, 15 mM EGTA, 1 mM DTT and 1 mM PMSF. The mixture was then centrifuged at 500*g* for 4 min and the supernatant was discarded. Beads were then washed four times with washing buffer (0.5% Triton X-100, 50 mM Tris-Cl (pH 7.5), 100 mM NaCl, 15 mM EGTA, 1 mM DTT and 1 mM PMSF), and then the bound protein complexes were boiled in SDS sample buffer (containing guanidine hydrochloride) at 95 °C for 5 min and subsequently analysed by western blot.

ATP determination and mitochondrial respiration.

Oxygen consumption rates were assessed using a Seahorse XF^e96 extracellular flux analyzer (Agilent Technologies) as previously described[63]. MEFs were seeded on XF^e96-well plates 24–48 h before the experiment. Cells were placed in assay medium for 1 h (unbuffered DMEM supplemented with 1 mM glutamine, 10 mM glucose and 1 mM pyruvate, pH 7.4). After recording baseline oxygen consumption rates, cells were challenged with 1 μM oligomycin, 500 nM FCCP and 1 μM rotenone/ antimycin A to reveal basal, maximal and ATP-coupled respiration. Whole-cell ATP levels were calculated in cells seeded 24–48 h before treatments. To measure ATP in tissues, isolated mitochondria or cells, we used a luciferase detection kit (A22066, Invitrogen) following the manufacturer's instructions and normalized to protein levels. Cytosolic or mitochondrial ATP in single-cell live imaging was calculated using the FRET ratio from the indicated cell lines that were transfected with either cytosolic or mitochondria-tagged ATP probes[28]. Cells were imaged using a Leica SP5 microscope with a 453 nm laser, with an emission of 460–490 nm for CFP and 520–540 nm for YFP/FRET. Mitochondrial complex I and III activity was estimated through the evaluation of the ROS production in total or mitochondrial liver samples. ROS production was measured using 25 μM CM-H_2DCFDA (485 nm, 530 nm) with the Biotek Synergy HT plate reader as previously described[64]. Then, 25 μg of isolated mitochondria were added to 100 μl of KCl respiration buffer with 5 mM pyruvate and 2.5 mM malate as oxidative substrates at 37 °C. ROS production was calculated as the maximum dichlorofluorescein fluorescence following 30 min of incubation, expressed in arbitrary fluorescence units.

Animal studies.

This study was carried following the strict recommendations in the Guide for the Care and Use of Laboratory Animals of the National Institutes of Health. Animal protocols were

approved by the Committee on the Ethics of Animal Experiments of the University of Chile (number: 0833 FMUCH). Mice were housed under a 12 h:12 h light:dark cycle with access to food and water ad libitum. *Ern1* mutant mice, either RNase[42] or kinase[43] were bred with Mx-Cre mice[41]. IRE1α deletion was achieved by injecting intraperitoneal 150 μg of poly:IC (Invivogen) three times every two days. Sex- and age-matched male and female mice ranging in age from two to six months were used for this study.

A glucose tolerance test was performed in eight-week-old male mice as reported[48]. Mice were starved overnight before being injected with 1.5 g kg^{-1} of glucose. Glucose levels were obtained from tail vein blood with one touch ultrastrips (Johnson & Johnson). Mx-Cre-negative poly:IC-injected age-matched littermates were used in all experiments. All samples were included in analysis unless they fell more than two standard deviations from the mean.

Metabolomics studies.

Metabolic studies were carried out in liver tissue samples as previously described[65]. About 30 mg of tissue for each condition was first weighted and solubilized into 1.5 ml polypropylene microcentrifuge tubes with ceramic beads using 1 ml of cold lysate buffer (methanol:water:chloroform, 9:1:1, −20 °C). They were then homogenized three times for 20 s at 5,500 r.p.m. using a Precellys 24 tissue homogenizer (Bertin Technologies), followed by centrifugation (10 min at 15,000*g*, 4 °C). The upper phase of the supernatant was split into two parts: the first 150 μl was used for the gas chromatography coupled with mass spectrometry (GC–MS) using vial injection, the other 250 μl was used for the ultrahigh pressure liquid chromatography coupled with mass spectrometry (UHPLC–MS). The GC–MS aliquots (150 μl) were evaporated and dried, and 50 μL of methoxyamine (20 mg ml^{-1} in pyridine) was added, after which the aliquots were stored at room temperature in the dark for 16 h. The subsequent day, 80 μl of MSTFA was added and final derivatization was performed at 40 °C for 30 min. Samples were then directly injected into GC–MS. For the LC–MS aliquots, the collected supernatant was evaporated in microcentrifuge tubes at 40 °C in a pneumatically assisted concentrator (Techne DB3). The LC–MS dried extracts were solubilized with 450 μl of MilliQ water and aliquoted in three microcentrifuge tubes (100 μl) for each LC method and one microcentrifuge tube for backup. Aliquots for analysis were transferred in LC vials and injected into UHPLC–MS or kept at −80 °C until injection. Afterwards, manual verification and quality control protocols were performed. An extended version of these methods is available on request, 243 metabolites were obtained in total. Analysis of relevant pathways that were altered was obtained by analysing the significantly altered metabolites (comparing experimental groups) using MetaboAnalystR[66].

Statistics and reproducibility.

Results were statistically compared using the Kruskal–Wallis ANOVA for unpaired groups followed by multiple comparison posttests (Tukey multiple comparison test). Student's *t*-tests were performed for unpaired or paired groups; one- or two-tailed experiments are indicated in each figure legend. Analysis was performed using GraphPad software. All experiments were performed at least three times independently and some blots were repeated at least twice.

Reporting Summary.

Further information on research design is available in the Nature Research Reporting Summary linked to this article.

Data availability

Mass spectrometry data have been deposited in ProteomeXchange (PXD013313). Metabolomics data have been deposited as a Mendeley dataset at https://data.mendeley.com/ (https://doi.org/10.17632/dtdf7wk3mb.1). Source data for Figs. 1–7 and for Supplementary Figs. 1–4 and 7 have been provided in Supplementary Table 6. Source data for Fig. 6 and Supplementary Fig. 6 have been provided in Supplementary Tables 3 and 4. Source data for Fig. 7 and Supplementary Fig. 7 can be found in Supplementary Table 5. All data that support the findings of this study are available from the corresponding author on reasonable request.

Supplementary Material

Refer to Web version on PubMed Central for supplementary material.

Acknowledgements

We thank S. Lavandero, D. Rojas-Rivera and M. Chiong for initial feedback in this project and for sharing reagents, T. Iwawaki for providing IRE1α null animals and L. Qi for providing IRE1α mutant constructs, G. Hajnoczky for MAM linker constructs, T. Calì and M. Brini for the SPLICS constructs, D. Ron for providing IRE1α null MEFs, J. Ponce for animal care, and N. Bossut, F. Aprahamian, A. Florizoone, M. Crabbe, K. Welkenhuyzen, C. Villablanca, T. Vervliet and T. Luyten for their support. This work was funded by FONDECYT 1140549, FONDAP program 15150012, the Millennium Institute P09–015-F and the European Commission R&D MSCA-RISE 734749 (to C.H.); the Michael J. Fox Foundation for Parkinson's Research target validation grant number 9277, FONDEF ID16I10223, FONDEF D11E1007, US Office of Naval Research-Global N62909–16-1–2003, US Air Force Office of Scientific Research FA9550–16-1–0384, ALSRP Therapeutic Idea Award AL150111, Muscular Dystrophy Association 382453, Seed grant Leading House for the Latin American Region, Switzerland and CONICYT-Brazil 44192½016–7 (to C.H.), FONDECYT 1160332 and FONDAP15150012 (to J.C.C.); the Spanish Ministry of Economy and Competitiveness SAF2014–52228-R, Unidad de Excelencia María de Maeztu, funded by the MINECO (ref: MDM-20140370) and Fundació la Marató de TV3 20134030 (to R.V.); NIH NS095892 (to R.L.W.); FONDECYT 11180825 (to H.U.); FONDECYT 3150113 and EMBO ASTF 385–2016 (to A.C.-S.); FONDECYT 3140355 (to E.R.-F.); FONDECYT 3140458 and 11170291 (to F.J.); FONDECYT 3180427 (to Y.H.); FONDECYT 3190738 (to A.S.-C.); FONDECYT 11170546 and CONICYT PAI 77170091 (to C.T.-R.); R01DK113171, R01CA198103 and R01DK103185 (to R.J.K.); FONDECYT 1150766 (to F.A.C.); the Research Council KU Leuven grant OT14/101 (to G.B.); the Research Foundation – Flanders (FWO) G.0C91.14N, G.0A34.16N and the FWO Scientific Research Community "Ca^{2+} signaling in health, disease and therapy" W0.019.17 (to G.B.); FWO (G049817N, G076617N) and KU Leuven (C16/15/073) (to P.A.); a FWO doctorate fellowship (to M.K.); the European Union's Horizon 2020 research and innovation programme under the Marie Sklodowska-Curie grant 675448 (to M.L.S.); CONICYT fellowship PCHA/Doctorado Nacional/2016–21160232 (to M.G.-Q.); the George E. Hewitt Foundation for a postdoctoral fellowship (to D.E.M.); Ligue contre le Cancer (équipe labellisée); Agence National de la Recherche – Projets blancs; under the frame of E-Rare-2, the ERA-Net for Research on Rare Diseases; Association pour la recherche sur le cancer; Cancéropôle Ile-de-France; Chancelerie des universités de Paris (Legs Poix), Fondation pour la Recherche Médicale; a donation from Elior; the European Research Area Network on Cardiovascular Diseases (MINOTAUR), Gustave Roussy Odyssea, the European Union Horizon 2020 Project Oncobiome; Fondation Carrefour; High-end Foreign Expert Program in China (GDW20171100085); Institut National du Cancer; Inserm (HTE); Institut Universitaire de France; LeDucq Foundation; the LabEx Immuno-Oncology; the RHU Torino Lumière; the Seerave Foundation; the SIRIC Stratified Oncology Cell DNA Repair and Tumor Immune Elimination; and the SIRIC Cancer Research and Personalized Medicine (to G.K.).

References

1. Rwland AA & Voeltz GK Endoplasmic reticulum–mitochondria contacts: function of the junction. Nat. Rev. Mol. Cell Biol. 13, 607–625 (2012). [PubMed: 22992592]

2. Wang M & Kaufman RJ Protein misfolding in the endoplasmic reticulum as a conduit to human disease. Nature 529, 326–335 (2016). [PubMed: 26791723]
3. Hetz C & Papa FR The unfolded protein response and cell fate control. Mol. Cell 69, 169–181 (2018). [PubMed: 29107536]
4. Oakes SA & Papa FR The role of endoplasmic reticulum stress in human pathology. Annu. Rev. Pathol. Mech. Dis. 10, 173–194 (2015).
5. Wu H, Carvalho P & Voeltz GK Here, there, and everywhere: the importance of ER membrane contact sites. Science 361, eean5835 (2018).
6. Gutiérrez T & Simmen T Endoplasmic reticulum chaperones tweak the mitochondrial calcium rheostat to control metabolism and cell death. Cell Calcium 70, 64–75 (2017). [PubMed: 28619231]
7. Carreras-Sureda A, Pihán P & Hetz C Calcium signaling at the endoplasmic reticulum: fine-tuning stress responses. Cell Calcium 70, 24–31 (2017). [PubMed: 29054537]
8. Phillips MJ & Voeltz GK Structure and function of ER membrane contact sites with other organelles. Nat. Rev. Mol. Cell Biol. 17, 69–82 (2015). [PubMed: 26627931]
9. Rizzuto R, De Stefani D, Raffaello A & Mammucari C Mitochondria as sensors and regulators of calcium signalling. Nat. Rev. Mol. Cell Biol. 13, 566–578 (2012). [PubMed: 22850819]
10. Giorgi C, Marchi S & Pinton P The machineries, regulation and cellular functions of mitochondrial calcium. Nat. Rev. Mol. Cell Biol. 19, 713–730 (2018). [PubMed: 30143745]
11. Izzo V, Bravo-San Pedro JM, Sica V, Kroemer G & Galluzzi L Mitochondrial permeability transition: new findings and persisting uncertainties. Trends Cell Biol. 26, 655–667 (2016). [PubMed: 27161573]
12. de Brito OM & Scorrano L Mitofusin 2 tethers endoplasmic reticulum to mitochondria. Nature 456, 605–610 (2008). [PubMed: 19052620]
13. Ngoh GA, Papanicolaou KN & Walsh K Loss of mitofusin 2 promotes endoplasmic reticulum stress. J. Biol. Chem. 287, 20321–20332 (2012).
14. Muñoz JP & Zorzano A Mfn2 modulates the unfolded protein response. Cell Cycle 13, 491–492 (2014). [PubMed: 24419149]
15. Carreras-Sureda A, Pihán P & Hetz C The unfolded protein response: at the intersection between endoplasmic reticulum function and mitochondrial bioenergetics. Front. Oncol. 7, 55 (2017). [PubMed: 28421160]
16. Verfaillie T et al. PERK is required at the ER-mitochondrial contact sites to convey apoptosis after ROS-based ER stress. Cell Death Differ. 19, 1880–1891 (2012). [PubMed: 22705852]
17. Muñoz JP et al. Mfn2 modulates the UPR and mitochondrial function via repression of PERK. EMBO J. 32, 2348–2361 (2013). [PubMed: 23921556]
18. Lebeau J et al. The PERK arm of the unfolded protein response regulates mitochondrial morphology during acute endoplasmic reticulum stress. Cell Rep. 22, 2827–2836 (2018). [PubMed: 29539413]
19. Hetz C The unfolded protein response: controlling cell fate decisions under ER stress and beyond. Nat. Rev. Mol. Cell Biol. 13, 89–102 (2012). [PubMed: 22251901]
20. Hayashi T & Su TP Sigma-1 receptor chaperones at the ER-mitochondrion interface regulate Ca^{2+} signaling and cell survival. Cell 131, 596–610 (2007). [PubMed: 17981125]
21. Mori T, Hayashi T, Hayashi E & Su T-P Sigma-1 receptor chaperone at the ER-mitochondrion interface mediates the mitochondrion-ER-nucleus signaling for cellular survival. PLoS ONE 8, e76941 (2013). [PubMed: 24204710]
22. Wieckowski MR, Giorgi C, Lebiedzinska M, Duszynski J & Pinton P Isolation of mitochondria-associated membranes and mitochondria from animal tissues and cells. Nat. Protoc. 4, 1582–1590 (2009). [PubMed: 19816421]
23. Sepulveda D et al. Interactome screening identifies the ER luminal chaperone Hsp47 as a regulator of the unfolded protein response transducer IRE1α. Mol. Cell 69, 238–252 (2018). [PubMed: 29351844]
24. Bae YS et al. Identification of a compound that directly stimulates phospholipase C activity. Mol. Pharmacol. 63, 1043–1050 (2003). [PubMed: 12695532]

25. Suzuki J et al. Imaging intraorganellar Ca2+ at subcellular resolution using CEPIA. Nat. Commun. 5, 4153 (2014). [PubMed: 24923787]
26. Oakes SA et al. Proapoptotic BAX and BAK regulate the type 1 inositol trisphosphate receptor and calcium leak from the endoplasmic reticulum. Proc. Natl Acad. Sci. USA 102, 105–110 (2005). [PubMed: 15613488]
27. Thrower EC et al. Interaction of luminal calcium and cytosolic ATP in the control of type 1 inositol (1,4,5)-trisphosphate receptor channels. J. Biol. Chem. 275, 36049–36055 (2000).
28. Imamura H et al. Visualization of ATP levels inside single living cells with fluorescence resonance energy transfer-based genetically encoded indicators. Proc. Natl Acad. Sci. USA 106, 15651–15656 (2009).
29. Mihaylova MM & Shaw RJ The AMPK signalling pathway coordinates cell growth, autophagy and metabolism. Nat. Cell Biol. 13, 1016–1023 (2011). [PubMed: 21892142]
30. Cárdenas C et al. Essential regulation of cell bioenergetics by constitutive $InsP_3$ receptor Ca^{2+} transfer to mitochondria. Cell 142, 270–283 (2010). [PubMed: 20655468]
31. Friedman JR et al. ER tubules mark sites of mitochondrial division. Science 334, 358–362 (2011). [PubMed: 21885730]
32. Westermann B Bioenergetic role of mitochondrial fusion and fission. Biochim. Biophys. Acta Bioenerg. 1817, 1833–1838 (2012).
33. Cogliati S et al. Mitochondrial cristae shape determines respiratory chain supercomplexes assembly and respiratory efficiency. Cell 155, 160–171 (2013). [PubMed: 24055366]
34. Bravo R et al. Increased ER-mitochondrial coupling promotes mitochondrial respiration and bioenergetics during early phases of ER stress. J. Cell Sci. 124, 2143–2152 (2011). [PubMed: 21628424]
35. Csordás G et al. Imaging interorganelle contacts and local calcium dynamics at the ER-mitochondrial interface. Mol. Cell 39, 121–132 (2010). [PubMed: 20603080]
36. Giacomello M & Pellegrini L The coming of age of the mitochondria–ER contact: a matter of thickness. Cell Death Differ. 23, 1417 (2016). [PubMed: 27341186]
37. Cieri D et al. SPLICS: a split green fluorescent protein-based contact site sensor for narrow and wide heterotypic organelle juxtaposition. Cell Death Differ. 25, 1–15 (2017).
38. Xue Z et al. A conserved structural determinant located at the interdomain region of mammalian inositol-requiring enzyme 1α. J. Biol. Chem. 286, 30859–30866 (2011).
39. Fan G et al. Gating machinery of $InsP_3R$ channels revealed by electron cryomicroscopy. Nature 527, 336–341 (2015). [PubMed: 26458101]
40. Yamazaki H, Chan J, Ikura M, Michikawa T & Mikoshiba K Tyr-167/Trp-168 in type 1/3 inositol 1,4,5-trisphosphate receptor mediates functional coupling between ligand binding and channel opening. J. Biol. Chem. 285, 36081–36091 (2010).
41. Kuhn R, Schwenk F, Aguet M & Rajewsky K Inducible gene targeting in mice. Science 269, 1427–1429 (1995). [PubMed: 7660125]
42. Iwawaki T, Akai R, Yamanaka S & Kohno K Function of IRE1 alpha in the placenta is essential for placental development and embryonic viability. Proc. Natl Acad. Sci. USA 106, 16657–16662 (2009).
43. Zhang K et al. The unfolded protein response transducer IRE1α prevents ER stress-induced hepatic steatosis. EMBO J. 30, 1357–1375 (2011). [PubMed: 21407177]
44. Sala-Vila A et al. Interplay between hepatic mitochondria-associated membranes, lipid metabolism and caveolin-1 in mice. Sci. Rep. 6, 27351 (2016).
45. Poston CN, Krishnan SC & Bazemore-Walker CR In-depth proteomic analysis of mammalian mitochondria-associated membranes (MAM). J. Proteom. 79, 219–230 (2013).
46. Jouaville LS, Pinton P, Bastianutto C, Rutter GA & Rizzuto R Regulation of mitochondrial ATP synthesis by calcium: evidence for a long-term metabolic priming. Proc. Natl Acad. Sci. USA 96, 13807–13812 (1999).
47. Tubbs E et al. Mitochondria-associated endoplasmic reticulum membrane (MAM) integrity is required for insulin signaling and is implicated in hepatic insulin resistance. Diabetes 63, 3279–3294 (2014). [PubMed: 24947355]

48. Arruda AP et al. Chronic enrichment of hepatic endoplasmic reticulum-mitochondria contact leads to mitochondrial dysfunction in obesity. Nat. Med. 20, 1427–1435 (2014). [PubMed: 25419710]
49. Hetz C, Chevet E & Oakes SA Proteostasis control by the unfolded protein response. Nat. Cell Biol. 17, 829–838 (2015). [PubMed: 26123108]
50. Hetz C & Glimcher LH Fine-tuning of the unfolded protein response: assembling the IRE1alpha interactome. Mol. Cell 35, 551–561 (2009). [PubMed: 19748352]
51. Arruda AP & Hotamisligil GS Calcium homeostasis and organelle function in the pathogenesis of obesity and diabetes. Cell Metab. 22, 381–397 (2015). [PubMed: 26190652]
52. Fink EE et al. XBP1-KLF9 axis acts as a molecular rheostat to control the transition from adaptive to cytotoxic unfolded protein response. Cell Rep. 25, 212–223 (2018). [PubMed: 30282030]
53. Song M et al. IRE1α–XBP1 controls T cell function in ovarian cancer by regulating mitochondrial activity. Nature 562, 423–428 (2018). [PubMed: 30305738]

References

54. Calfon M et al. IRE1 couples endoplasmic reticulum load to secretory capacity by processing the XBP-1 mRNA. Nature 415, 92–96 (2002). [PubMed: 11780124]
55. Rodriguez DA et al. BH3-only proteins are part of a regulatory network that control the sustained signalling of the unfolded protein response sensor IRE1α. EMBO J. 31, 2322–2335 (2012). [PubMed: 22510886]
56. Hetz C et al. Proapoptotic BAX and BAK modulate the unfolded protein response by a direct interaction with IRE1α. Science 312, 572–576 (2006). [PubMed: 16645094]
57. Ryno LM et al. Characterizing the altered cellular proteome induced by the stress-independent activation of heat shock factor 1. ACS Chem. Biol. 9, 1273–1283 (2014). [PubMed: 24689980]
58. Parys JB et al. Rat basophilic leukemia cells as model system for inositol 1,4,5-trisphosphate receptor IV, a receptor of the type II family: functional comparison and immunological detection. Cell Calcium 17, 239–249 (1995). [PubMed: 7664312]
59. Wuytack F, Eggermont JA, Raeymaekers L, Plessers L & Casteels R Antibodies against the non-muscle isoform of the endoplasmic reticulum Ca2(+)-transport ATPase. Biochem. J. 264, 765–769 (1989). [PubMed: 2482734]
60. Nixon-Abell J et al. Increased spatiotemporal resolution reveals highly dynamic dense tubular matrices in the peripheral ER. Science 354, aaf3928 (2016).
61. Tovey SC & Taylor CW High-throughput functional assays of IP3-evoked Ca2+ release. Cold Spring Harb. Protoc. 2013, 930–937 (2013). [PubMed: 24086049]
62. Luyten T, Bultynck G, Parys JB, De Smedt H & Missiaen L Measurement of intracellular Ca2+ release in permeabilized cells using 45Ca2+. Cold Spring Harb. Protoc. 2014, 289–294 (2014). [PubMed: 24591686]
63. Xian S, Shang D, Kong G & Tian Y FOXJ1 promotes bladder cancer cell growth and regulates Warburg effect. Biochem. Biophys. Res. Commun. 495, 988–994 (2018). [PubMed: 29129693]
64. Jara C, Aránguiz A, Cerpa W, Tapia-Rojas C & Quintanilla RA Genetic ablation of tau improves mitochondrial function and cognitive abilities in the hippocampus. Redox Biol. 18, 279–294 (2018). [PubMed: 30077079]
65. Pietrocola F et al. Metabolic effects of fasting on human and mouse blood in vivo. Autophagy 13, 567–578 (2017). [PubMed: 28059587]
66. Xia J & Wishart DS Web-based inference of biological patterns, functions and pathways from metabolomic data using MetaboAnalyst. Nat. Protoc. 6, 743–760 (2011). [PubMed: 21637195]

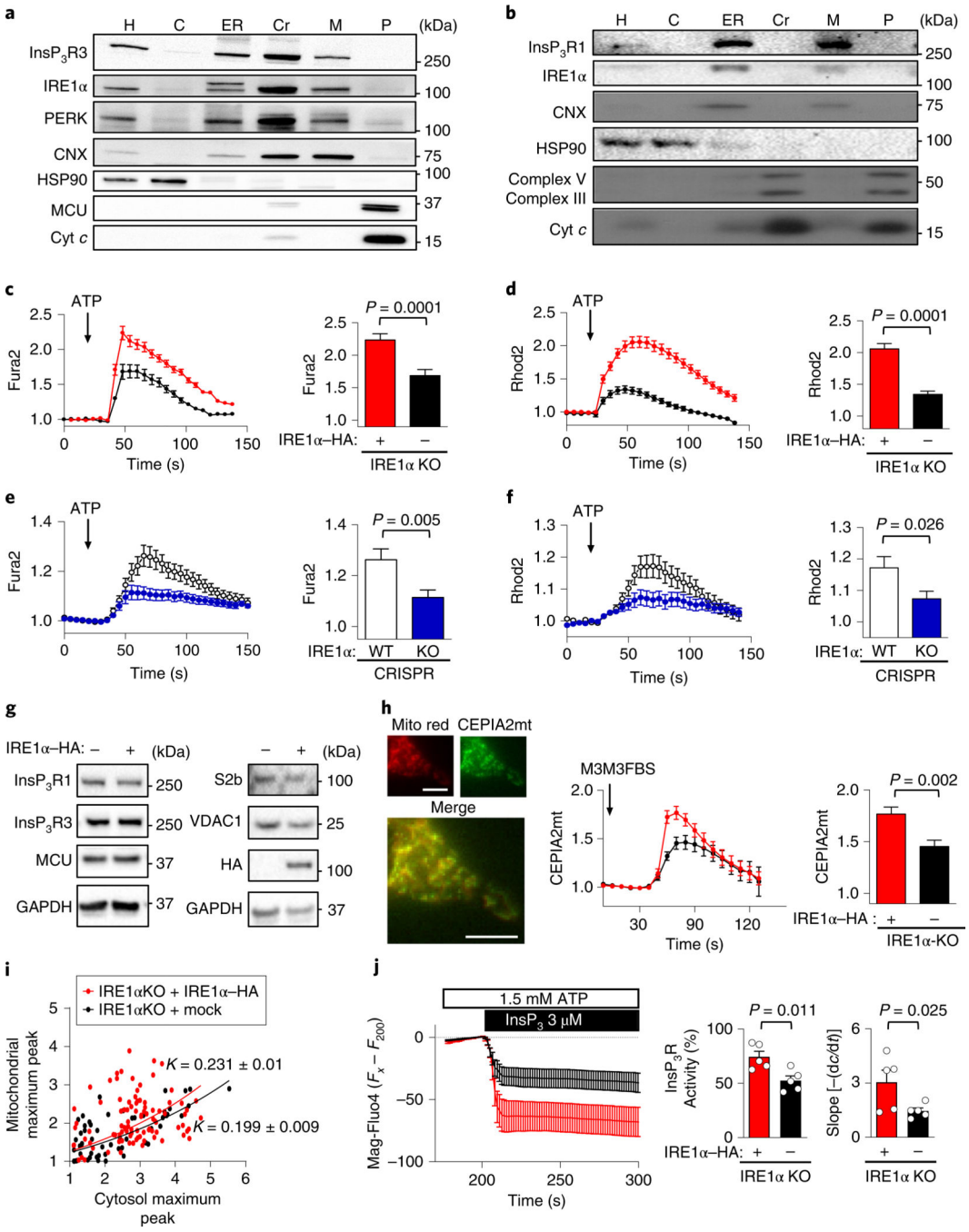

Fig. 1 |. IRE1α is located at MAMs and enhances mitochondrial calcium uptake.

a, IRE1α KO cells reconstituted with IRE1α–HA were processed to obtain purified MAM fractions followed by western blot analysis of indicated proteins ($n = 3$ independent experiments). H, homogenate; C, cytosol; Cr, crude mitochondria; M, MAMs; P, pure mitochondria; Cyt c, cytochrome c; CNX, calnexin. **b**, Liver extracts were processed to obtain subcellular fractions enriched for MAMs and analysed by western blot ($n = 9$ independent experiments). **c**,**d**, IRE1α KO cells reconstituted with IRE1α–HA or mock control were simultaneously imaged for calcium signals in the cytosol (Fura2; **c**) and

mitochondria with Rhod2 (**d**). Left, the Fura2 ratio (**c**) and mean Rhod2 intensity (**d**) of normalized data before and after ATP is added; arrow, 100 μM ATP. Right, the data for the maximum peak are shown (total cells analysed: mock, $n = 116$ cells; IRE1α–HA, $n = 138$ cells). **e**,**f**, Similar experiments for Fura2 (**e**) and Rhod2 (**f**) were performed in CRISPR control and IRE1α KO cells (total cells analysed: control, $n = 129$ cells; IRE1α KO, $n = 117$ cells). WT, wild type. **g**, Indicated cell lines were processed for western blot analyses to monitor the levels of indicated proteins ($n = 4$ independent experiments). **h**, IRE1α null and control cells were imaged for calcium levels in mitochondria by transiently expressing CEPIA2mt mitochondrial calcium probe (left) after addition of 50 μM M3M3FBS (arrow), (Mito red; Mitochondrila Ds-Cherry control). Scale bars, 10 μm. Right, maximum CEPIA2mt intensity for every cell analysed (mock, $n = 14$ cells; IRE1α–HA, $n = 14$ cells). **i**, Maximum peaks from Fura2/Rhod2 measurements from samples described in **c** and **d** were calculated using nonlinear regression analyses to determine the correlation constant (K) and s.e.m. (mock, $K = 0.199 \pm 0.009$; IRE1α–HA, $K = 0.231 \pm 0.01$). **j**, Cells were imaged for calcium levels in the ER after loading with Mag-Fluo4 in permeabilized cells followed by stimulation with $InsP_3R$ ($n = 5$ independent experiments; left). Middle, percentage activity for $InsP_3R$ for each condition normalized to maximum release (ionomycin). Right, the first derivative was calculated. Data in **c**–**f**,**h**–**j** are mean ± s.e.m. Statistical differences were detected using two-tailed unpaired Student's t-tests except for **j**; right, which was one-tailed. Source data for statistical analyses are provided in Supplementary Table 6.

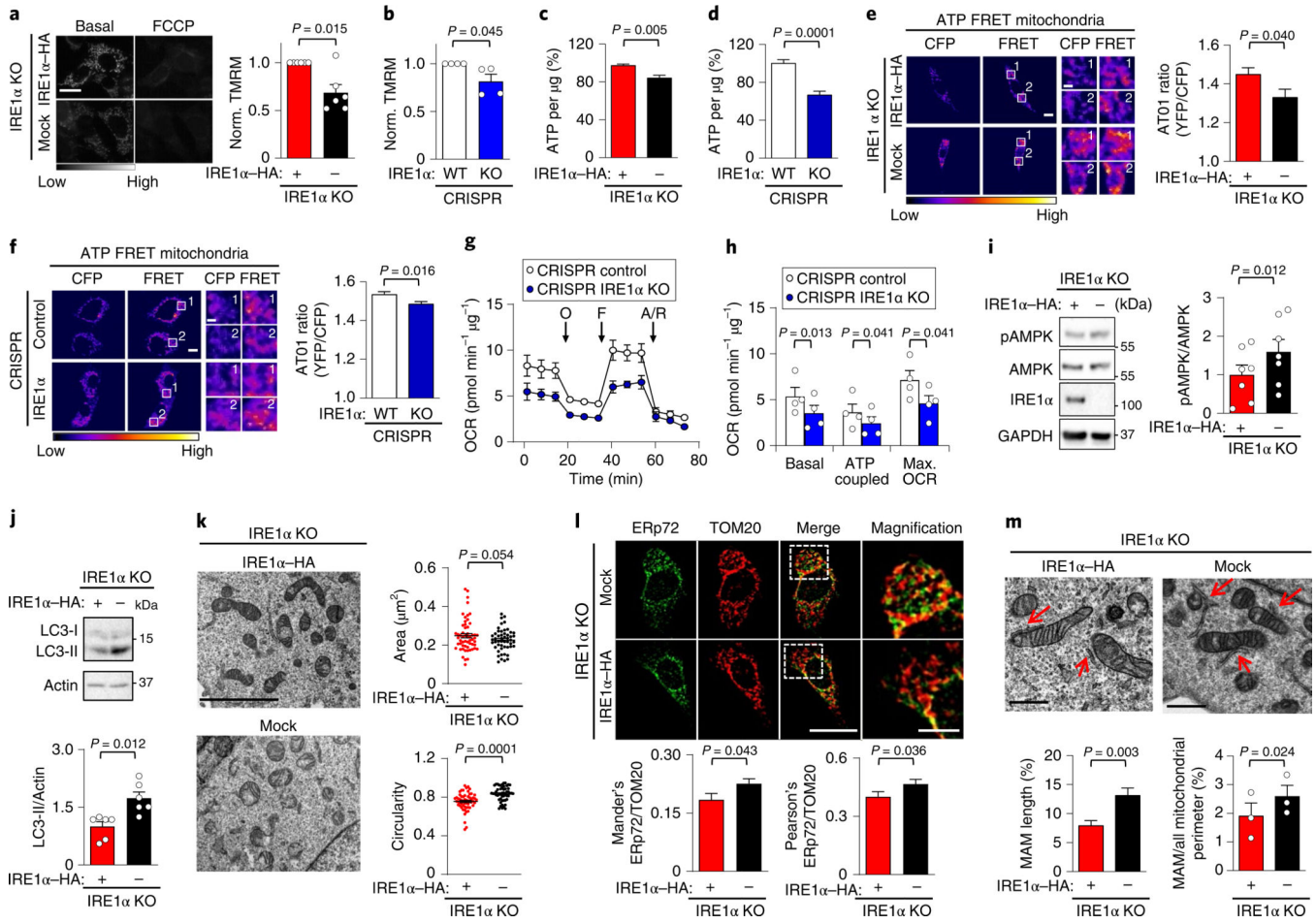

Fig. 2 |. IRE1α expression bursts basal mitochondrial bioenergetics.

a, IRE1α KO cells that were reconstituted with either IRE1α–HA or an empty vector (mock) were imaged for TMRM signals before and after addition of 1 μM FCCP (carbonyl cyanide-p-trifluoromethoxyphenylhydrazone) (left). Scale bar, 20 μm. Right, mean TMRM intensity normalized to IRE1α–HA cells ($n = 6$ independent experiments). **b**, CRISPR control and IRE1α KO cells were analysed as described in **a** ($n = 4$ independent experiments). **c**,**d**, Percentage of ATP of the indicated cells using a luminescence assay ($n =$ 18 biologically independent samples). **e**,**f**, ATP levels were measured in the indicated cell lines using the AT01 mitochondrial (yellow fluorescent protein (YFP)/cyan fluorescent protein (CFP)) FRET probe FRET labeling stands for 440 nm excitation emmited in YFP channel. White numbers indicate regions of interest (left). Right, quantification of YFP/CFP ratio excited at 440 nm (mock, $n = 52$ cells; IRE1α–HA, $n = 58$ cells; control, $n = 145$ cells; IRE1α KO, $n = 151$ cells). Scale bars, 10 μm and 2 μm. **g**,**h**, The indicated cell lines were analysed for oxygen consumption rate (OCR). O, 1 μM oligomycin, F, 0.5 μM FCCP; A/R = 1 μM antimycin/rotenone ($n = 4$ independent experiments). **i**, pAMPK was analysed in the indicated cells using western blots (left) and normalized to total AMPK levels (right; $n = 6$ independent experiments). **j**, Determination of LC3-II levels in the indicated cell lines using western blots (left), followed by quantification normalizing to actin (right; $n = 6$ independent experiments). **k**, TEM-derived morphological parameters of mitochondria were obtained

from indicated cells. Scale bar, 4 μm (left). Right, the data represent the area in μm^2 and circularity (mock, $n = 52$ cells; IRE1α–HA, $n = 58$ cells). **l**, Cells were stained for ERp72 and TOM20 by indirect immunofluorescence (left) followed by colocalization quantification (right; Mander's index: mock, $n = 33$ cells; IRE1α–HA, $n = 40$ cells; Pearson's index: mock, $n = 68$ cells; IRE1α–HA, $n = 78$ cells). Scale bar, 20 μm and 5 μm. **m**, The indicated cells were imaged using TEM to visualize MAMs (pointed with red arrows) (left) using two quantification methods (right; mock, $n = 38$ contacts; IRE1α–HA, $n = 30$ contacts). Scale bars, 500 nm. Data in **a**–**m** are mean ± s.e.m. Statistical differences detected with one-tailed (**k**) or two-tailed unpaired Student's *t*-tests. A Wilcoxon signed-rank test was applied in **a**–**d** and paired Student's *t*-tests were applied in **h**,**i**,**m** (right panel). Source data for statistical analyses are provided in Supplementary table 6.

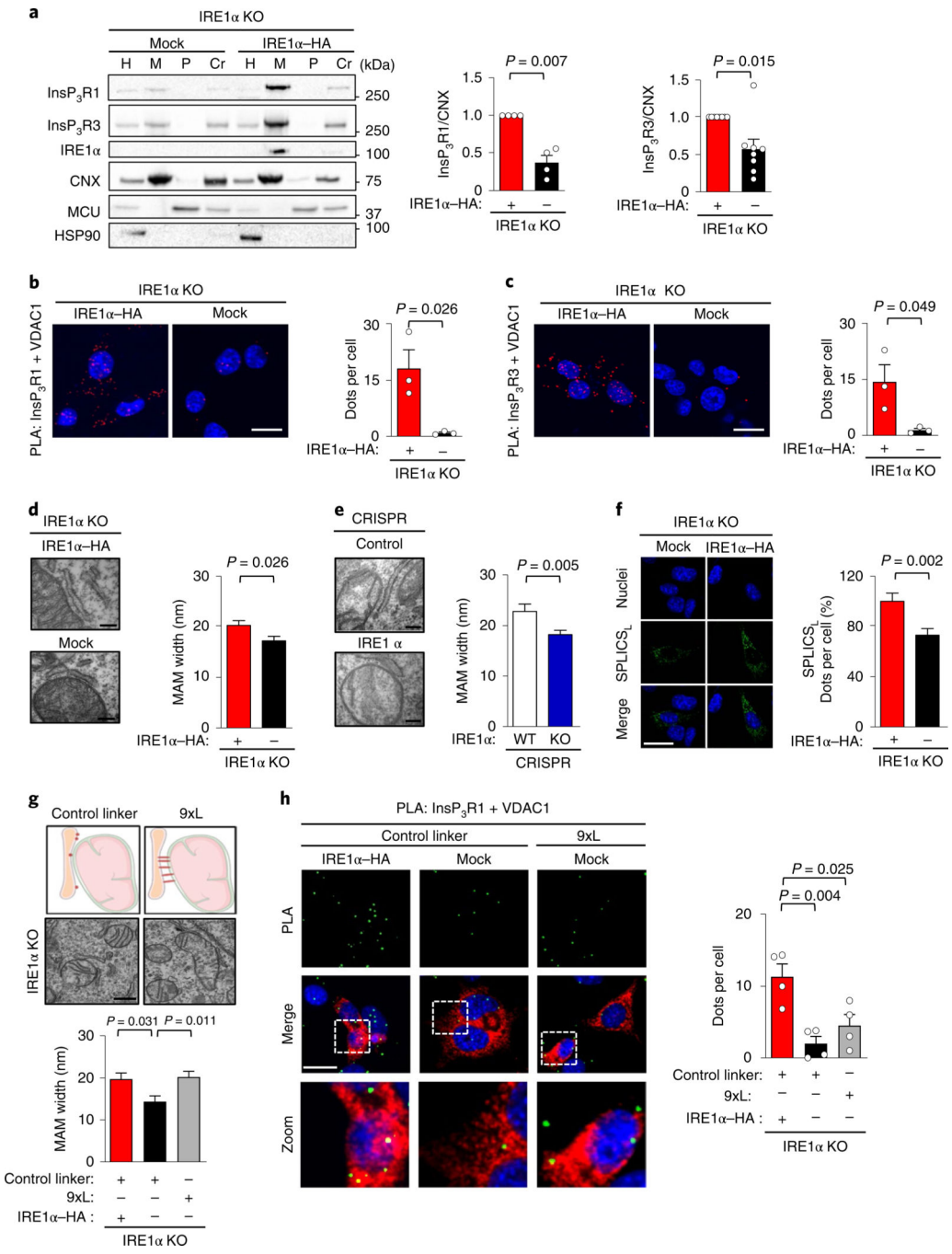

Fig. 3 |. IRE1α controls the distribution of $InsP_3Rs$ at MAMs.

a, Indicated cells were processed to obtain subcellular fractions and analysed using western blots. Right, quantification of the MAM fractions for the indicated proteins ($InsP_3R1$, $n = 4$; $InsP_3R1$, $n = 8$ independent experiments). **b**,**c**, Cells described in **a** were stained with a PLA (red) and DAPI (Blue) using anti-$InsP_3R1$ (**b**) or anti-$InsP_3R3$ (**c**) antibodies paired with anti-VDAC1 antibodies. Scale bars, 20 μm (left). Right, quantification of the number of positive PLA dots per cell ($n = 3$ independent experiments). **d**, Cells were imaged using TEM (left) to calculate ER to mitochondrial width (right; $n = 3$ independent experiments;

mock, $n = 46$ contacts; IRE1α–HA, $n = 30$ contacts). Scale bars, 200 nm. **e**, CRISPR control and IRE1α KO cells were were imaged using TEM (left) to calculate ER to mitochondrial width (right; $n = 3$ independent experiments; CRISPR control, $n = 27$ contacts; CRISPR IRE1α KO, $n = 47$ contacts). Scale bars, 200 nm. **f**, The same cells as described in **a** were transiently transfected with $SPLICS_L$ to visualize MAMs with a width of 40–50 nm (left). Nuclei were stained with DAPI. Scale bar, 25 μm. Right, quantification of $SPLICS_L$ signal as dots per cell ($n = 5$ independent experiments; total cells analysed: mock, $n = 41$ cells; IRE1α–HA, $n = 38$ cells). **g**, Schematic representation and representative TEM images of indicated cells transiently expressing either a AKAP1 (34–63)-linker 9x-mRFP (9xL) construct or a control linker construct. Scale bar, 500 nm (top). MAM width was determined by TEM (bottom; mock control linker, $n = 14$ contacts; IRE1α–HA control linker, $n = 12$ contacts; mock 9xL, $n = 15$ contacts). **h**, Cells described in **g** were stained with PLA (green) and DAPI (blue) to measure the close proximity between $InsP_3R1$ and VDAC1 proteins (left) in mRFP positive cells. Right, the number of dot counts per cell was quantified ($n = 4$ independent experiments) Scale bars, 20 μm. Data in **a**–**h** are mean ± s.e.m. Statistical differences were detected using one-way ANOVA and Tukey post-tests for multiple comparison (**g**,**h**), two-tailed Student's *t*-tests (**b**–**f**) or Wilcoxon signed-rank test (**a**). Source data for statistical analyses are provided in Supplementary Table 6.

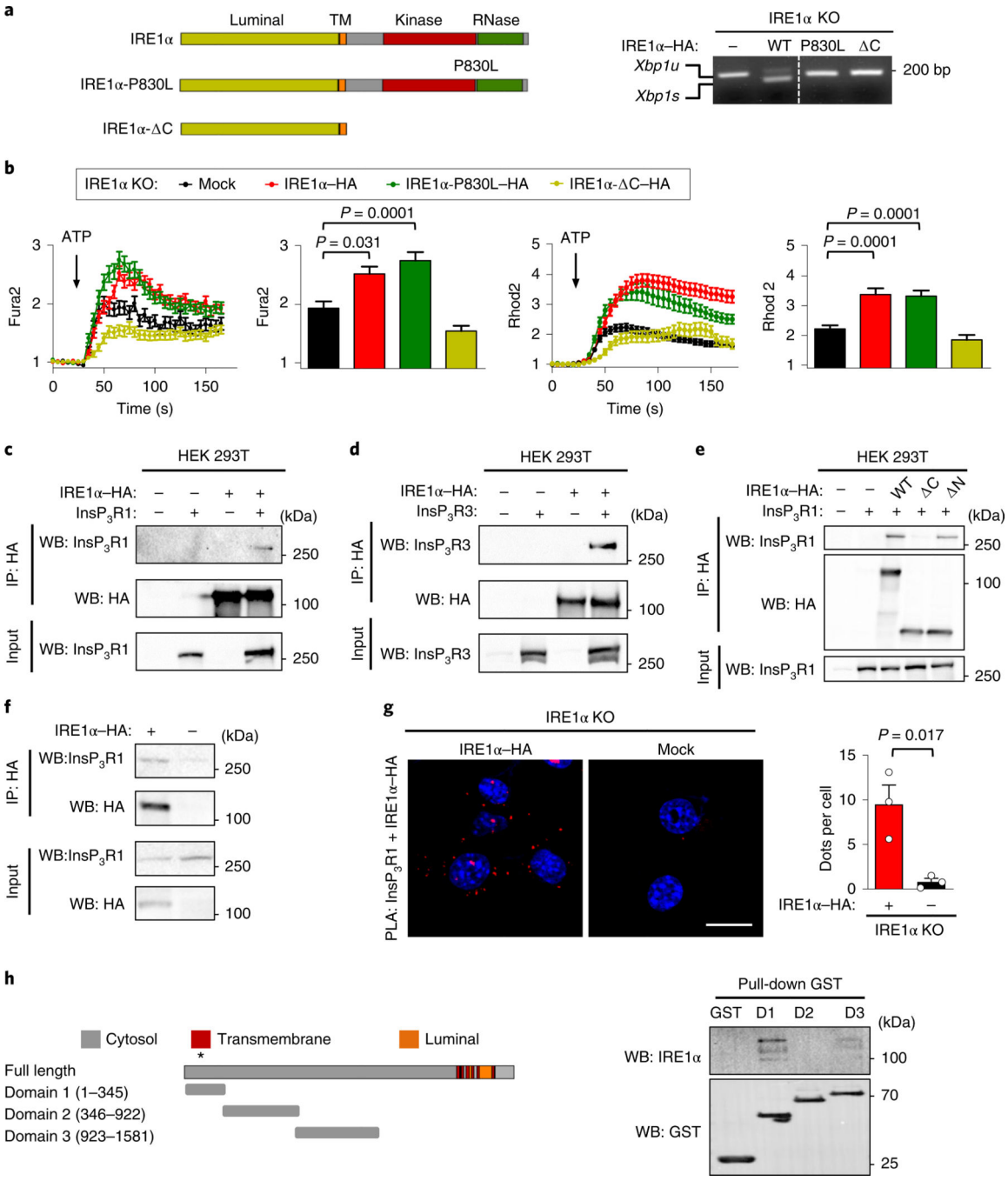

Fig. 4 |. IRE1α physically interacts with $InsP_3Rs$ and controls mitochondrial calcium uptake independent of its enzymatic activities.

a, Schematic of IRE1α structure and the mutants analysed (left) (TM; transmembrane domain). Right, the indicated cell lines were treated with 0.1 μg ml^{-1} tunicamycin for 4 h and then *Xbp1* mRNA splicing was evaluated using PCR analysis. The agarose gel image was sliced to eliminate irrelevant lanes. *Xbp1u*, unspliced *Xbp1s*, spliced ($n = 2$ independent experiments). **b**, Calcium levels in the cytosol after ATP stimulation were analysed in IRE1α KO cells reconstituted with the indicated constructs. Arrow, 100 μM ATP (left; Fura2; $n = 4$

independent experiments; total cells analysed: mock, $n = 131$ cells; IRE1α–HA, $n = 149$ cells; IRE1α-P830L–HA, $n = 120$ cells; IRE1α-ΔC–HA, $n = 97$ cells). The maximum peak for the normalized Fura2 ratio was measured (middle). The same cells were imaged simultaneously with Rhod2 to measure mitochondrial calcium uptake. Arrow, 100 μM ATP (right two panels). **c**–**e**, HEK293T cells were transiently transfected with the indicated constructs and immunoprecipitation (IP) was performed using anti-HA antibodies. Western blot (WB) analysis was performed for the indicated proteins in immunoprecipitations and total input (**c**, $n = 3$ independent experiments; **d**,**e** are representative of two independent experiments). **f**, The indicated MEF cell lines were processed for immunoprecipitation using anti-HA antibodies. Western blot analysis was performed for the indicated proteins in immunoprecipitations and total input. **g**, Cells described in **f** were stained for PLA (red) and DAPI (blue) using anti-$InsP_3R1$ antibodies paired with anti-HA antibodies and analysed by confocal microscopy. Scale bar, 20 μm (left). Right, the number of dots per cell were quantified ($n = 3$ independent experiments). **h**, Schematic of $InsP_3R1$ domains used to generate recombinant proteins and perform in vitro pull-down assays (left; the asterisk indicates that residues 167–169 and 267 are relevant for channel function). Right, in vitro pull-down assay for purified GST-fused domains of $InsP_3R1$ with recombinant IRE1α cytosolic portion (IRE1α-ΔN) followed by western blot analysis (D1, domain 1; D2, domain 2; D3, domain 3; $n = 3$ independent experiments). Data in **b** and **g** are mean ± s.e.m. Statistical differences were detected using two-tailed unpaired Student's *t*-test (**g**) or ANOVA with Tukey multiple comparison test (**b**). Source data for statistical analyses are provided in Supplementary Table 6.

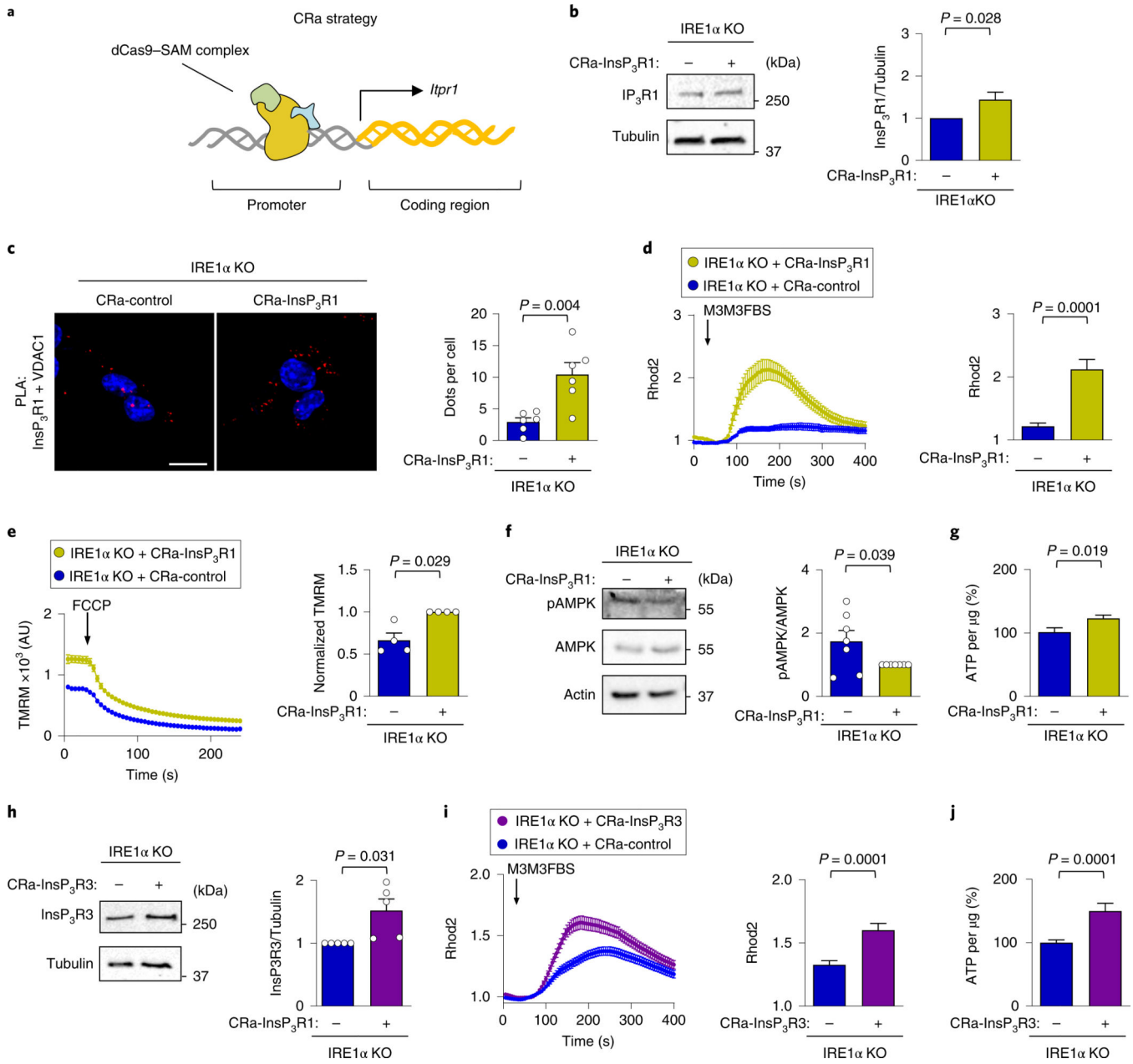

Fig. 5 |. Upregulation of endogenous $InsP_3Rs$ rescue mitochondrial calcium uptake in IRE1α-deficient cells.

a, Strategy to generate CRa particles using the synergistic activator mediators and sgRNA complex. **b**, IRE1α KO cells were generated that stably express either a CRa that targets the $InsP_3R1$ promoter or a control vector. Representative western blot analysis of the indicated proteins was performed to confirm $InsP_3R1$ upregulation ($n = 10$ independent experiments). **c**, The cells described in **a** were stained with a PLA (red) DAPI (blue) using anti- $InsP_3R1$ and anti-VDAC1 antibodies, and were analysed by confocal microscopy. Scale bar, 20 µm (left). Right, the number of dots per cell were quantified ($n = 6$ independent experiments). **d**, CRa-$InsP_3R1$ or CRacontrol cells were imaged with Rhod2 to measure mitochondrial calcium uptake. Arrow, stimulation using 50 µM M3M3FBS (left). Right, the maximum

peak for normalized Rhod2 was calculated (total cells analysed: CRa-InsP_3R1, $n = 46$ cells; CRa-control, $n = 42$ cells). **e**, CRa-InsP_3R1 or CRa-control cells were imaged for mitochondrial membrane potential after TMRM staining (left). Arrow, stimulation with 1 μM FCCP; AU, arbitrary units. Right, normalized TMRM intensity ($n = 4$ independent experiments). **f**, pAMPK and total AMPK levels were determined in CRa-InsP_3R1 or CRa-control cells using western blot (left). Right, quantification of the pAMPK/AMPK ratio ($n = 7$ independent experiments). **g**, The indicated cells were lysed and ATP levels were determined using a luminescence assay ($n = 13$ biologically independent experiments). **h**, IRE1α KO cells were generated that stably express either a CRa that targets the InsP_3R3 promoter or a control vector. Representative western blot analysis of the indicated proteins was performed to confirm InsP_3R3 upregulation ($n = 5$ independent experiments). **i**, The indicated cells were imaged with Rhod2. Arrow, stimulation with 50 μM M3M3FBS (left). Right, the maximum peak for the normalized Rhod2 was calculated (total cells analysed: CRa-InsP_3R1, $n = 132$ cells; CRa-control, $n = 112$ cells). **j**, ATP levels were determined in the indicated cells using a luminescence assay ($n = 25$ biologically independent experiments). Data in **b**–**j** are mean ± s.e.m. Statistical differences were detected with unpaired Student's *t*-tests (**c**,**d**,**g**,**i**,**j**) or Wilcoxon signed-rank test (**b**,**e**,**f**,**h**). Source data for statistical analyses are provided in Supplementary Table 6.

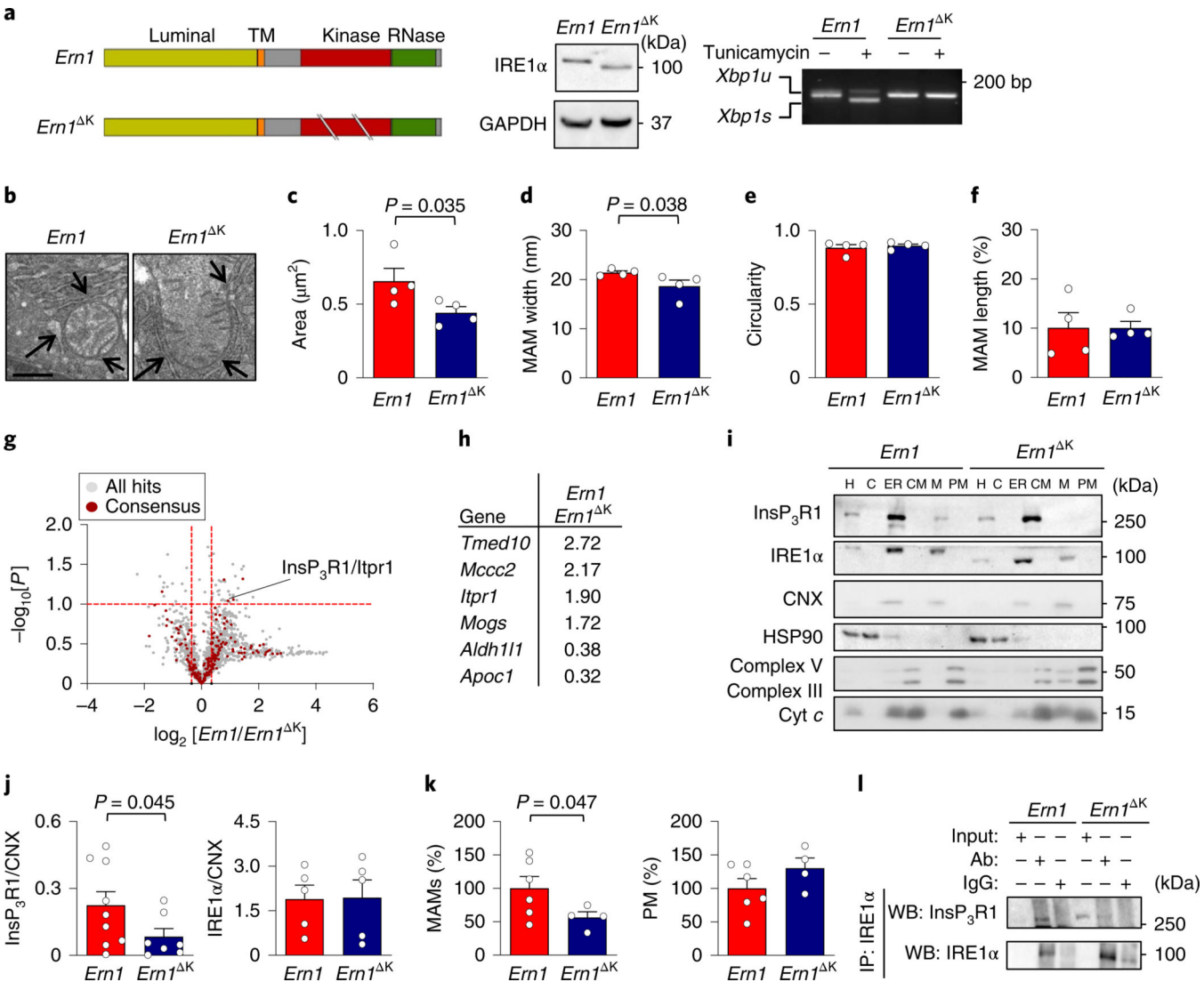

Fig. 6 |. IRE1α is required for the localization of InsP$_3$R1 at MAMs in vivo.

a, Schematic of *Ern1* structure (the gene encoding IRE1α) (TM; transmembrane domain) and the strategy to delete the kinase domain (*Ern1*$^{\Delta K}$; left). Middle, livers from *Ern1* control and *Ern1*$^{\Delta K}$ mice were processed for western blot analysis to measure the levels of indicated proteins ($n = 3$ independent experiments). Right, mice were intraperitoneally injected with 1 mg kg^{-1} of tunicamycin or vehicle for 6 h. *Xbp1s* mRNA splicing was evaluated by RT–PCR analysis of cDNA obtained from total liver extracts. **b**–**f**, *Ern1* and *Ern1*$^{\Delta K}$ livers were processed for TEM analysis (**b**) to determine morphological parameters including mitochondrial area (arrows indicate MAMs, scale bar, 500 nm) (**c**), MAM width (**d**), mitochondrial circularity (**e**) and MAM length (**f**; $n = 4$ animals per group). **g**, *Ern1* and *Ern1*$^{\Delta K}$ MAM fractions were processed for quantitative mass spectrometry analysis (see Methods). The volcano plot shows all of the detected proteins (grey) and those that are known to be present at MAMs (red dots; $n = 3$ animals per group). **h**, A summary of statistically significant hits observed in the proteomic screening of MAMs. **i**,**j**, *Ern1* and *Ern1*$^{\Delta K}$ liver samples were processed to obtain subcellular fractions, and were analysed by

western blot for the indicated proteins (**i**). Quantification of protein expression was performed for the indicated proteins by normalizing to calnexin (CNX; **j**; *Ern1*, $n = 9$ animals; *Ern1*$^{\Delta K}$, $n = 7$ animals). **k**, The protein content (in mg) from liver MAM fractions (left) or pure mitochondria (right) was quantified and normalized by total liver extract (in g) to obtain the percentage of MAM proteins in the liver (*Ern1*, $n = 6$ animals; *Ern1*$^{\Delta K}$, $n = 4$ animals). **l**, Liver homogenates from *Ern1* and *Ern1*Δ^{K} were immunoprecipitated for IRE1α and analysed for the indicated proteins by western blot. Ab, antibody (representative of three independent experiments). Data in **c**–**f**,**j** and **k** are mean ± s.e.m. Statistical differences were detected using two-tailed unpaired Student's *t*-tests (**c**,**d**). For **j**,**k** one-tailed Student's *t*-tests were applied. Source data for statistical analyses are provided in Supplementary Table 6.

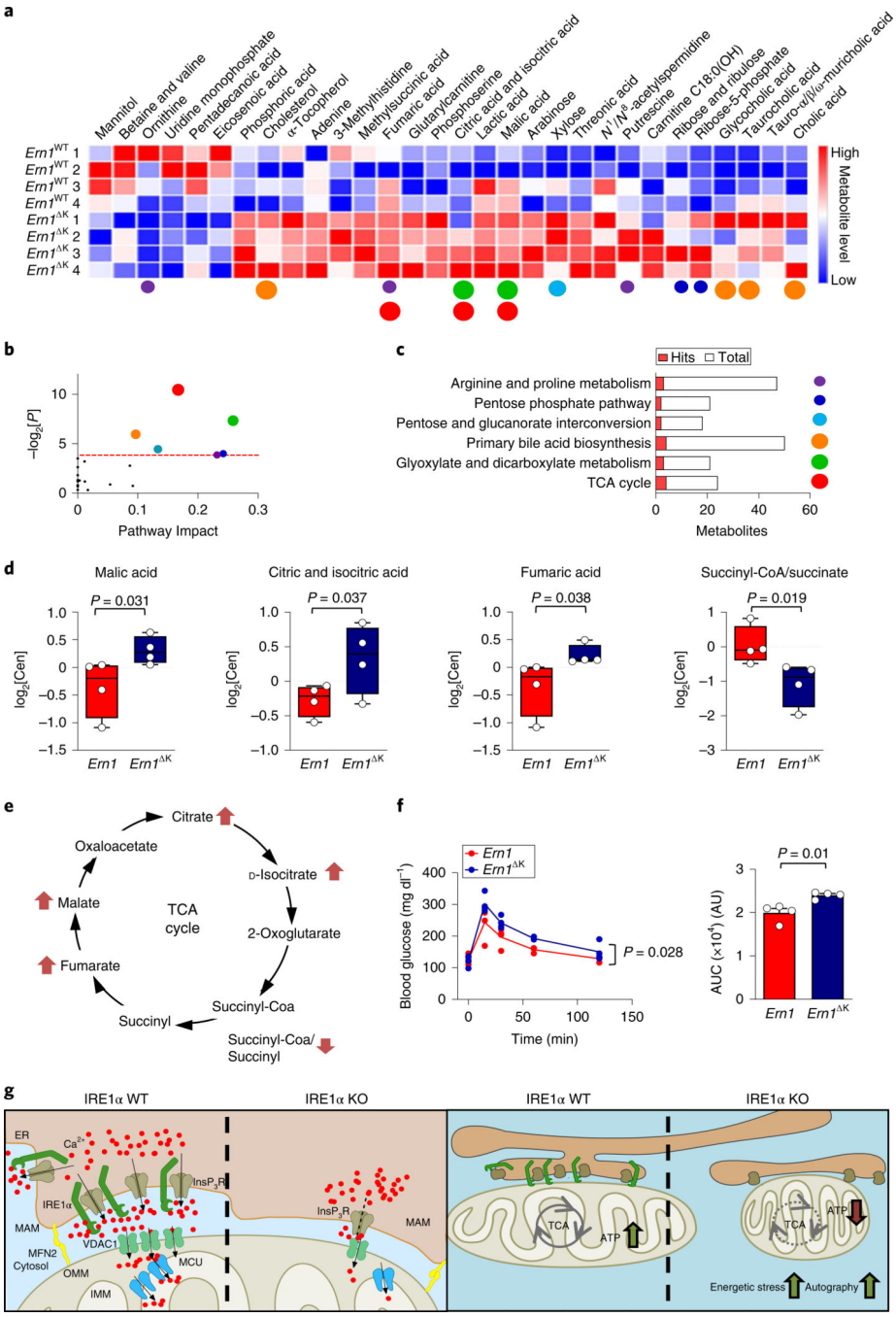

Fig. 7 |. IRE1α expression regulates liver metabolism.

a, *Ern1* and *Ern1*$^{\Delta K}$ liver samples were processed for metabolomics studies ($n = 4$ animals per group). The heat map for the metabolites indicates significantly different metabolite levels in each experimental animal. **b**, Pathway analysis and statistical significance (two-tailed Student's *t*-test) for the metabolites shown in **a**. **c**, The affected pathways and main hits from **a** are indicated. Altered metabolites and their associated pathways are indicated using the same colour code (coloured dots, size stands for *P* value as in **b**)) in **a**–**c**. **d**, Whisker and dot plots of the indicated metabolites of the TCA, indicating median and

quartiles derived from samples in **a** ($n = 4$ animals per group) levels represent the log2 of the normalized area in a.u. **e**, Schematic of the TCA cycle. Metabolites with increased or decreased levels in *Ern1* and *Ern1*$^{\Delta K}$ samples are indicated by arrows. **f**, Glucose tolerance test in *Ern1* control and *Ern1*$^{\Delta K}$ mice (left). Right, data represent the area under the curve (AUC) for the whole glucose tolerance test ($n = 4$ animals per group). **g**, Proposed model: IRE1α expressed at MAMs docks the $InsP_3Rs$ at the mitochondrial–ER contact sites—possibly through a physical interaction, which may enhance $InsP_3R$ channel activity. The presence of IRE1α at MAMs favours calcium transfer into the mitochondria and bursts in ATP production. IRE1α deficiency leads to a metabolic stress condition that is characterized by the constitutive activation of AMPK, enhanced compensatory autophagy and altered mitochondrial morphology. Data are mean ± s.e.m. Statistical differences were detected with one-tailed (**d**) or two-tailed Student's *t*-tests (**f**) or two-way ANOVA (**f**). Source data for statistical analyses are provided in Supplementary Table 6.